Tribology International 186 (2023) 108545

Contents lists available at ScienceDirect

Tribology International

journal homepage: www.elsevier.com/locate/triboint

Response of elastic/viscoelastic layers on an elastic half-space in rolling contacts: Towards a new modeling approach for elastohydrodynamic lubrication

Y. Zhao [a,*], H.C. Liu [b,c], G.E. Morales-Espejel [d], C.H. Venner [a]

[a] Faculty of Engineering Technology, University of Twente, Enschede, 7500AE, The Netherlands
[b] State Key Laboratory of Solid Lubrication, Lanzhou Institute of Chemical Physics, Chinese Academy of Sciences, Lanzhou, 730000, China
[c] Qingdao Key Laboratory of Lubrication Technology for Advanced Equipment, Qingdao Center of Resource Chemistry and New Materials, Qingdao, 266100, China
[d] SKF Research and Technology Development, Meidoornkade 14, Houten, 3922AE, The Netherlands

ARTICLE INFO

Keywords:
Contact mechanics
Elastic/viscoelastic layered contact
Foundation (Winkler) approach
Stress analysis
EHL
Layer deformation

ABSTRACT

The 3D quasi-static contact problem of a rigid sphere rolling on an elastic half-space covered by a thin viscoelastic/elastic layer is studied as representative of soft layered contacts in engineering, physics, and biomedical applications, as well as for its potential merit to model Elasto-Hydrodynamically Lubricated (EHL) contacts in specific EHL film behavior suggested in earlier research. The viscoelastic layer behavior is modeled with a standard linear solid (SLS) model with a single relaxation time. Two approaches are used, the foundation (Winkler) reduced model assuming unidirectional stress–strain behavior normal to the surface only and the Papkovich–Neuber potential model which, based on the complete Navier–Cauchy equations, accounts for non-local support and bending effects. The models are validated against literature and compared. Whereas coated/layered contact problem studies mostly consider relatively thick coatings, and results focus on the pressure distribution and the contact area size, in this paper we consider layers with a thickness much smaller than the contact radius, i.e. of the order of a thickness of a conventional EHL film. The details of the layer deformation, pressure profiles and subsurface stresses are presented and interpreted in terms of the underlying physics, in particular the thin layer limit common also in thin fluid layers. It is shown that two dimensionless parameters, the ratio of the elastic modulus between the layer and the substrate and the ratio of the layer thickness to the corresponding Hertz contact width, dominate the systematic response for elastic layered contact problems. And four dimensionless parameters with two extras, the Deborah number based on the Hertz contact width and the ratio of the two elastic limits of the SLS viscoelastic material, are needed and analyzed for viscoelastic layered contacts. The results presented provide a good framework for the understanding and interpretation of the effects of viscoelastic layers on the deformation and pressure distribution of contact problems. Finally, the capability of actually modeling EHL film behavior via a viscoelastic layer suggested by van Emden et al. (2017) is discussed.

1. Introduction

A large variety of contacts operate with hard/soft coatings (e.g. DLC, TiAlN, PTFE), thin films (e.g. grease thickener rich layer [1,2], anti-wear additive induced tribofilm [3]) and/or material inhomogeneities (e.g. inclusions, anisotropic grains [4]) with the mechanical properties of the close-to-surfaces material being different from the bulk. This is in particular of interest in bio-mechanics, such as soft (viscoelastic) layered contact problems regarding joint cartilage and human skin [5]. In addition, thin layer coatings are ubiquitous in both hard and soft Elasto-Hydrodynamically Lubricated (EHL). One may argue that the film itself can also be seen as a thin layer, see van Emden et al. [6]. In general, lubricated contacts have to operate under increasingly severe conditions by using low-viscosity lubricants, reduced lubricant supply and higher temperatures/loads, which all lead to thinner and possibly intermittent films. In these circumstances small scale effects such as local high pressure, rheology of lubricants and the particular composition, crystallography and topology of the material may play an important role in the lubricant film formation and (surface) failure. In particular, contacts are operating close to, or even in the mixed lubrication regime. In this respect the lubrication modeling ability of

* Corresponding author.
E-mail addresses: y.zhao-7@utwente.nl (Y. Zhao), c.h.venner@utwente.nl (C.H. Venner).

https://doi.org/10.1016/j.triboint.2023.108545
Received 5 March 2023; Received in revised form 11 April 2023; Accepted 21 April 2023
Available online 4 May 2023

the continuum Reynolds based solution is quite limited in terms of intermittent contacts and complex fluid rheology. Van Emden et al. [6] suggested that these lubrication problems may be modeled as layered dry contact problems, i.e. not from the viewpoint of a (continuous) thin fluid film but from the viewpoint of a viscoelastic interface layer forming a local support (Winkler model).

The concept of viscoelastic layer modeling for EHL or even mixed lubrication may be supported by the following physical rheological features of a thin lubricating film. First, both pressure-induced bulk glass transition [7,8] and confinement-induced nano-rheological solidification [9,10] have been recognized in highly-loaded EHL contacts. The lubricant film behaves as a viscoelastic material with a long relaxation time or a "soft" deformable elastic solid with a yield stress when it is far into the glassy state [8,11,12], e.g. with the viscosity in the order of 10^{12} Pas for inorganic liquids and about 10^{7} Pas for organic liquids [8]. In such cases, a pressure gradient may exist across the thin lubricating film [13], which may break the classical lubrication assumption (i.e. a constant pressure across the thin film) and thus limit the application of the Reynolds equation in modeling such problems. Second, in the case that the contact pressure is not high enough to induce glass transition, the lubricant in an EHL contact, owing to the high viscosity, still hardly exhibits any pressure driven flow and behaves as a near solid layer passing through the contact. Therefore, viscoelastic layer modeling may provide a new approach to model EHL and/or mixed lubrication by taking account of the complex mechanical–rheological properties of the lubricants. Note that viscoelastic layered (dry) contact problems are relatively easy to solve compared with the classical governing equations of "hard" EHL including (fluid–structure) interaction between the Reynolds equation and the solid deformation equation [14].

Regarding viscoelastic layer modeling, much work has been done in the field of contact mechanics, such as problems of a viscoelastic layer on a rigid [5,15–21], an elastic [6,22–29] or a viscoelastic [30,31] half-space, even though these studies were not intended to model EHL. Here, some work on the modeling of a viscoelastic layered elastic half-space in rolling contacts is introduced. In 1967, Batra and Ling [22], using a Fourier transform method, analyzed the stress–strain state for contact problems of a viscoelastic layer on an elastic half-space under a moving load. Kalker et al. [23,24] studied the contact of cylinders coated with viscoelastic layers under conditions of dry rolling friction theoretically and experimentally. Based on this work, Goryacheva et al. [25,26] performed an analytical analysis of a cylinder rolling/sliding on an elastic base coated with a viscoelastic layer. Recently, this two-dimensional (2D) line contact analysis was extended to 3D using the strip method to calculate the contact pressure distribution and the internal stresses [27]. Zhang and He et al. [28,29] proposed a semi-analytical model to investigate the response of a viscoelastic layer-elastic substrate system under both dry [28] and lubricated [29] conditions, including the pressure distribution, displacements, viscoelastic dissipation and subsurface stresses. Wallace et al. [32] studied the pressure and subsurface stress response in the contact of a rolling body on a viscoelastic multi-layered half-space. So far coated/layered contact problem studies mostly considered relatively thick coatings (usually larger than a quarter of the Hertz contact width a_0), and results focused on the pressure distribution and the subsurface stress. In this paper we consider layers with a thickness much smaller than the contact radius, i.e. of the order of a thickness of a conventional EHL film.

The published modeling and numerical methods for the study of the viscoelastic layered contacts can be classified into two main categories: (1) calculating the deformation of the viscoelastic layer and the elastic half-space separately [6,27]; (2) solving the displacement field of the integrated layered system using a fully coupled deformation modeling [28,29]. For the first approach, different models of varying accuracy and complexity have been developed, among which the simplest calculates the layer deformation using the constitutive equation of the viscoelastic layer applied uni-directionally to the normal direction, neglecting the tangential stress–strain interaction in the layer (local support). This approach traces back to Winkler's model [33], and is also referred to as foundation approach. The second method is based on the complete Navier–Cauchy equations, simultaneously considering layer(s) and substrate with specific interface conditions. In this study, both approaches were used. A simplified foundation (Winkler) reduced model as well as a Navier–Cauchy equations based potential model for full 3D deformation have been developed for thin viscoelastic layered contact problems. The models were verified with the simulation results published in the literature for both viscoelastic and elastic layered rolling contacts, as well as for consistency with a viscoelastic half-space in contact. It can also reduce to the Green's function based model developed by Carbone and Putignano et al. [17] when the substrate is rigid. The results of both models for (thin) elastic and viscoelastic layers on an elastic substrate are compared in particular with respect to the layer deformation and the pressure distribution.

The results presented in literature were mainly about the pressure distribution, the stress and the displacement fields for contacts with relatively thick layers. However, to address the question if the viscoelastic layer modeling could indeed be used for modeling EHL, the present study is carried out in the thin layer regime with layer thicknesses in the order of $a_0 \times O(10^{-3})$. Also, in addition to the parameters considered in other studies, the deformation behavior of the viscoelastic layer and the resulting layer profile are analyzed in this work with a parametric study using the potential model. Finally, to answer the question if and when a viscoelastic layer can exhibit EHL film characteristics, we also study the piezoviscous effect of viscoelastic layer with the simplified foundation approach. From the results it is concluded that typical EHL film shapes could be obtained by breaking the linear viscoelasticity assumption.

2. Viscoelastic modeling and formulation

Fig. 1 schematically shows the contact problem of a rigid sphere of radius R_0 rolling on a viscoelastic layered elastic half-space. This problem is relevant for both soft contacts and "hard" EHL contacts in which the viscoelastic layer may be used to represent the lubricant film or grease thickener layer. The rigid sphere and the layered substrate move at constant surface velocities v_1 and v_2, respectively, under a constant normal load W_0. The mean velocity of the two moving bodies is $v_m = (v_1 + v_2)/2$. The viscoelastic layer has a constant thickness l_0 and it is assumed to be perfectly bonded to the elastic half-space. The mechanical properties of the elastic half-space are characterized by the elastic modulus E^s and the Poisson ratio ν^s. The mechanical–rheological properties of the viscoelastic layer and the mathematical formulations of the contact problem are introduced in the following two sections.

2.1. Viscoelastic rheological model

A three-element standard linear solid (SLS) model in the Kelvin representation with a single relaxation time is used to characterize the viscoelastic behavior of the layer, see Fig. 2. The SLS model consists of two units in series: a linear spring of rigidity E_f, and a Kelvin–Voigt model of a spring E_s in parallel with a Newtonian dashpot of viscosity η_s. Even though it may not characterize all aspects of viscoelastic behavior of realistic materials quantitatively, it is well suited to explore the main features of the response of viscoelastic layered systems, as used in [23–28]. The model exhibits two extreme asymptotic cases. Firstly, the immediate elastic response in a very short time (e.g. in a steady rolling contact at high speed) is $E^c_\infty = E_f$. Secondly, at a very long time interval, e.g. in a steady rolling contact at very low speeds, the elastic response is $E^c_0 = 1/(1/E_f + 1/E_s)$. The relation between the two extreme elastic moduli is $E^c_\infty/E^c_0 = 1 + R_e$ with $R_e = E_f/E_s$.

The constitutive equation relating stress and strain is

$$\sigma + \beta\frac{\partial \sigma}{\partial t} = E^c_0[\epsilon + \tau\frac{\partial \epsilon}{\partial t}] \tag{1}$$

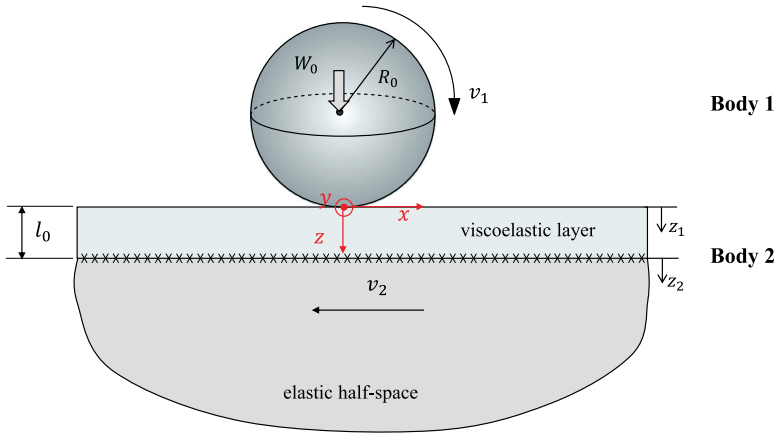

Fig. 1. Schematic of a rolling contact formed between a rigid sphere of radius R_0 and a layered elastic half-space at a constant load W_0.

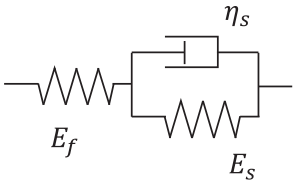

Fig. 2. Standard linear solid (SLS) viscoelastic model in Kelvin representation.

where τ is the constant (single) relaxation time $\tau = \eta_s/E_s$ and $\beta = \tau/(1+R_e)$. Analogous to the definition of the compliance (the reciprocal of the elastic modulus) in the theory of linear elasticity, the creep compliance function of the SLS model can be derived by solving Eq. (1) with a constant stress as input:

$$\varphi_c(t) = \frac{1}{E_0^c} + \left(\frac{1}{E_\infty^c} - \frac{1}{E_0^c}\right)e^{-\frac{t}{\tau}}. \tag{2}$$

Correspondingly, the relaxation modulus function can be obtained by solving Eq. (1) with a constant strain as input. However, it can be obtained more easily by the Fourier transform of Eq. (2), because in the frequency domain the relation between the creep compliance function and the relaxation function of viscoelastic materials is $\hat{\psi}_r(\omega) = [i\omega\hat{\varphi}_c(\omega)]^{-1}$ (see Appendix B). As a result, the relaxation modulus reads

$$\hat{\psi}_r(\omega) = 1/\left[\frac{1}{E_0^c} + \left(\frac{1}{E_\infty^c} - \frac{1}{E_0^c}\right)\frac{i\omega}{1+i\omega\tau}\right], \tag{3}$$

where ω is the frequency, i the imaginary unit, and the hat $\hat{}$ referring to the Fourier transform with respect to time t.

2.2. Mathematical formulation

In the same way as a classical Hertzian (elastic dry) contact problem [14], the viscoelastic layered rolling contact problem in Fig. 1 can be mathematically modeled by a gap height equation, a load balance equation and a complementary condition at the contact interface ($z_1 = 0$).

The gap height equation is:

$$h(x,y,t) = h_0(t) + \frac{(x-v_m t)^2}{2R_0} + \frac{y^2}{2R_0} + u(x,y,t) \tag{4}$$

where $h_0(t)$ is an indentation constant determined by the contact dynamics equation [34] and v_m the entrainment velocity.

Neglecting acceleration the dynamics equation reduces to the usual condition of load balance equation:

$$W_0(t) = \iint p(x,y,t)\mathrm{d}x\mathrm{d}y. \tag{5}$$

The complementary condition which needs to be satisfied is:

$$\begin{aligned} &h(x,y,t) = 0, p(x,y,t) > 0, \text{inside contact area,} \\ &h(x,y,t) > 0, p(x,y,t) = 0, \text{out of contact area.} \end{aligned} \tag{6}$$

The gap height equation, Eq. (4), consists of the undeformed gap shape approximating the surfaces of the contacting elements as paraboloids and their normal deformation. The load balance equation, Eq. (5), states that, neglecting the contact dynamics, the integral of the pressure should equal the externally applied load at any time. Finally, the actual problem to be solved is stated in Eq. (6) by the Hertz–Signorini–Moreau complementary condition, i.e. $ph = 0$. This means that when the gap is closed the pressure is positive, and when the gap is open, neglecting adhesion, the pressure is zero (ambient).

The gap height h, the pressure p, and the normal deformation u in Eqs. (4)~(6) are functions of time t, which also allows solutions of the dynamic response of the contact problem. However, the studied pure rolling contact, relative to the contact location, is steady-state (quasi-static). The time-dependent governing equations, Eqs. (4)~(6), in the inertial coordinate system can be transformed to a reference frame fixed to the contact location. In this reference system, the governing equations for the layered contact problem are the same as those for a common elastic dry (Hertzian) contact problem [14] with the variable x replaced by the transformed speed-dependent variable $x + v_m t$ to account for the motion of the moving bodies relative to the inertial coordinate system.

Compared to the Hertzian contact of two elastic bodies, the most challenging aspect of solving the viscoelastic layered contact problem is the evaluation of the deformation of the layered half-space, which includes two portions in the deformation term $u(x,y,t)$ of Eq. (4): the deformation of the viscoelastic layer and the elastic half-space. In the literature, two approaches have been used to evaluate the deformation of a viscoelastic layered half-space. The first is the foundation (Winkler) reduced model and the second the Navier–Cauchy equations based potential model. Since the modifications are mainly related to the deformation calculation by one of these methods, the following description focuses only on this aspect.

3. Foundation (Winkler) reduced model

For the foundation (Winkler) reduced model, the deformations of the layer and the substrate are calculated separately. The contact stresses/pressures at the interfaces of the layer-substrate and of the ball-layer are assumed to be the same (thin layer approximation, which is the equivalent of the lubrication assumption in fluid mechanics). The viscoelastic layer is represented by a discrete set of columns of the SLS representations with a uniform initial thickness l_0. Upon loading see Fig. 3, the displacement of each SLS column is assumed to be limited

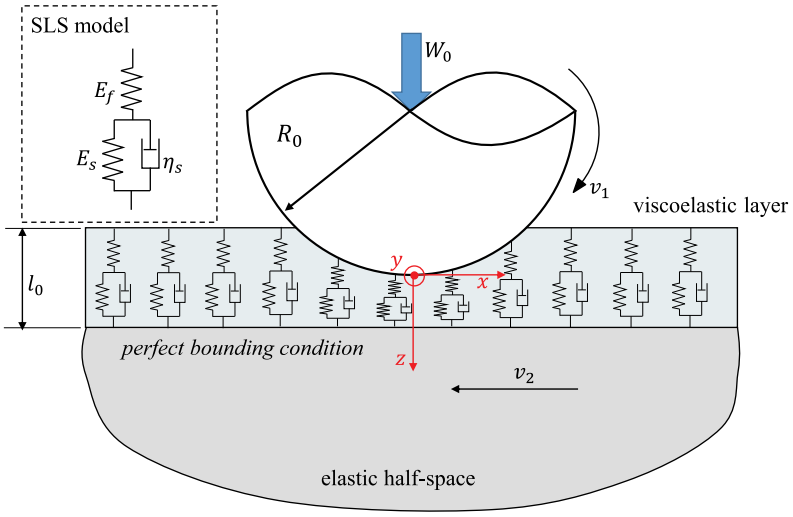

Fig. 3. Schematic representation of the foundation reduced approach to model the deformation of the viscoelastic layer for the layered contact problem shown in Fig. 1.

to the vertical direction (oedometric layer assumption), satisfying the constitutive equation of the SLS model, Eq. (1). This means that at a local spot/element the deformation at neighboring locations is neglected (local support). The deformation of the elastic substrate is calculated using the Boussinesq integral equation Eq. (9) based on the isotropic half-space assumption. The total deformation $u(x, y, t)$ is obtained by adding the deformation of the viscoelastic layer u^c and of the elastic half-space u^s.

3.1. Deformation equation

The viscoelastic layer deformation u^c is obtained by replacing the unidirectional strain ϵ and σ in the SLS constitutive equation Eq. (1) by u^c/l_0 and p, giving:

$$p(x,y,t) + \beta\frac{\partial p(x,y,t)}{\partial t} = \frac{E_0^c}{l_0}[u^c(x,y,t) + \tau\frac{\partial u^c(x,y,t)}{\partial t}]. \tag{7}$$

Eq. (7) evolves in time by showing the deformation process of the layer and finally reaches steady-state. It was also used by van Emden et al. but for Kelvin–Voigt model, see [6]. For a pure rolling contact in steady-state, Eq. (7) can be represented in the time-independent form by replacing x with $x + v_m t$ as reported in [35]. Afterwards, with the same notation, it is simplified to

$$p(x,y) + v_m\beta\frac{\partial p(x,y)}{\partial x} = \frac{E_0^c}{l_0}[u^c(x,y) + v_m\tau\frac{\partial u^c(x,y)}{\partial x}] \tag{8}$$

where x (and y) now refer to the coordinate relative to the contact location. Eq. (8) directly describes the steady-state solution in space and it will be used in the current study. Eq. (7) gives the same steady solution as Eq. (8) in the limit of infinite long time.

Based on the thin layer assumption, $p\big|_{z_1=0} = p\big|_{z_1=l_0}$. Hence, the deformation of the elastic substrate is

$$u^s(x,y) = \frac{1-(\nu^s)^2}{\pi E^s}\iint\frac{p(x',y')}{\sqrt{(x-x')^2+(y-y')^2}}\mathrm{d}x'\mathrm{d}y' \tag{9}$$

The total deformation $u(x, y)$ is the sum of the two contributions

$$u(x,y) = u^s(x,y) + u^c(x,y) \tag{10}$$

With the foundation model, the layer thickness after deformation can be obtained by

$$l(x,y) = l_0 - u^c(x,y) \tag{11}$$

3.2. Numerical methods

The governing equations Eqs. (4)~(6) with Eqs. (8)~(10) must be solved to achieve numerical solutions. Compared to the solution of the classical Hertzian dry contact problem, mainly an additional procedure is needed to calculate the deformation of the viscoelastic layer. The multigrid/multilevel elastic numerical solver published in [14] is taken as a starting point. The equations can be non-dimensionalized with the dimensionless variables:

$$\begin{aligned} &X = x/a_0, \quad Y = y/a_0, \quad P = p/p_{\mathrm{H}}, \quad U = u/\delta, \\ &\bar{l}_0 = l_0/\delta, \quad \delta = a_0^2/R_0 \\ &a_0 = \sqrt[3]{\frac{3W_0R_0(1-(\nu^s)^2)}{4E^s}}, \quad p_{\mathrm{H}} = \frac{3W_0}{2\pi a_0^2}, \quad \bar{E}_0 = E_0/p_{\mathrm{H}} \end{aligned} \tag{12}$$

where a_0 and p_{H} are the Hertzian contact parameters of the elastic half-space with modulus E^s. The dimensionless form of Eq. (8) is:

$$P(X,Y) + \frac{De}{1+Re}\frac{\partial P(X,Y)}{\partial X} = \frac{\bar{E}_0^c}{\bar{l}_0}[U^c(X,Y) + De\frac{\partial U^c(X,Y)}{\partial X}] \tag{13}$$

where $De = v_m\tau/a_0$ is the Deborah number relating the relaxation time to the passage time of surface point through half of the Hertzian contact zone. The dimensionless form of the other governing equations can be found in [14,36].

Accounting for the additional complexity of the viscoelastic deformation equation, a second order finite difference method was used on a uniform grid for the spatial discretization of the equations. As used for the elastic dry contact problem in [14] a distributive relaxation process was developed to solve Eqs. (4)~(6). Coarser grids were used in a multigrid cycle to accelerate the convergence to a grid independent rate [14]. The force balance equation was treated as a global constraint that was relaxed by adjusting the value of the mutual separation h_0 in this cycle. For the fast evaluation of the spatial integral transforms in Eq. (9), the multi-level multi-integration (MLMI) method was used [14]. With the full Multigrid (MG) algorithm the equations were solved to an error smaller than the discretization error.

A special consideration for the MG solution was that the calculation of the layer deformation was only performed on the finest grid level. For the foundation model, neighboring points are not linked at all, which leads to an instability (nonphysical behavior) of high frequency components in an MG cycle. This can be solved by requiring a smoothness on the scale of the coarse grid. The mean pressure values of four surrounding grid points were used to calculate the local deformation

of the layer. u^c was then obtained in the intermediate grid points by solving Eq. (8) numerically with the mean pressure values. In the MG calculation, five grid levels with $513 * 513$ equidistant grid points on the finest level were used. The computational domain was set to $(-8a_0, 4a_0)$ in the x direction to consider the delayed viscoelastic layer deformation at the outlet, while in the y direction the range of $(-4a_0, 4a_0)$ was large enough.

4. Potential model

The potential model does not rely on the assumptions of the foundation (Winkler) reduced model, i.e. the thin layer assumption and the oedometric layer assumption. A local (element) deformation in the layer is influenced by the entire pressure distribution rather than only having a local support. This leads to a general and precise solution to the studied contact problem. Numerically, the potential model can also be achieved based on a solver for elastic layered problems [37–40]. In the following, the elastic solver is introduced first, followed by an illustration of the application of the correspondence principle to the elastic solution to achieve the viscoelastic formulation that can be solved efficiently.

4.1. 3D elastic half-space and elastic layered solution

To obtain a 3D solution of the stress and displacement fields of an elastic contact problem, the Navier–Cauchy equation of elasticity [41] should be solved with the governing equations and the complementary boundary conditions. Without considering the acceleration and the body forces in equilibrium equation, the Navier–Cauchy equation reads

$$(\lambda + \mu)\nabla(\nabla \cdot \mathbf{u}) + \mu\nabla^2\mathbf{u} = 0 \tag{14}$$

where $\mu = \frac{E}{2(1+\nu)}$ and $\lambda = \frac{E\nu}{(1+\nu)(1-2\nu)}$ are the Lame's constants with E and ν the elastic modulus and the Poisson ratio of the material. Variations of λ and μ in the half-space domain, heterogeneous material, could be modeled [4].

To reduce the complexity of the computation when solving Eq. (14) in a 3D domain, potential functions are often used to represent the displacement. Define the displacement function $\mathbf{u}$ in Eq. (14) as [41],

$$2\mu\mathbf{u} = -4(1-\nu)\boldsymbol{\psi} + \nabla(\mathbf{r}\cdot\boldsymbol{\psi} + \phi) \tag{15}$$

where ϕ and ψ_i $(i = 1, 2, 3)$ are the Papkovich–Neuber elastic potentials with $\boldsymbol{\psi} = (\psi_1, \psi_2, \psi_3)$ and $\mathbf{r} = r(x, y, z)$. Substituting Eq. (15) in the strain–displacement relations

$$\epsilon_{ij} = \frac{1}{2}\left(\frac{\partial u_i}{\partial x_j} + \frac{\partial u_j}{\partial x_i}\right), \tag{16}$$

followed by substituting the result in the generalized Hooke's law:

$$\sigma_{ij} = \lambda\delta_{ij}\epsilon_{kk} + 2\mu\epsilon_{ij}, \tag{17}$$

the displacements and stresses for both the elastic layer and the elastic substrate are obtained as:

$$\begin{aligned} u_i &= \frac{1}{2\mu}\left[\phi_{,i} + x\psi_{1,i} + z\psi_{3,i} - (3-4\nu)\psi_i\right], \\ \sigma_{ij} &= \phi_{,ij} - 2\nu(\psi_{1,1} + \psi_{3,3})\delta_{ij} - (1-2\nu)(\psi_{i,j} + \psi_{j,i}) + x\psi_{1,ij} + z\psi_{3,ij}. \end{aligned} \tag{18}$$

where the indices i and j have values 1, 2, and 3 which correspond to x, y, and z, respectively. δ_{ij} is the Kronecker delta. The comma "," in Eq. (18) indicates differentiation with respect to the coordinate with the index following. Note that the above equations, Eqs. (14)~(18), hold for both the elastic layer and the elastic substrate. The stresses and displacements, σ_{ij} and u_i in the layer are taken as functions of (x, y, z_1), while in the half-space they are functions of (x, y, z_2).

With the superscript $k = c$ and $k = s$ indicating the coating and the substrate, respectively, for the present layered contact problem given in Fig. 1, the boundary conditions can be divided into two categories regardless of elastic or viscoelastic layer:

- On the top surface of the layer $z_1 = 0$, the pressure and shear stresses for frictionless rolling/sliding contacts are prescribed as following:

$$\begin{aligned} &\sigma^c_{33}(x, y, 0) = -p(x, y) \\ &\sigma^c_{31}(x, y, 0) = 0 \\ &\sigma^c_{32}(x, y, 0) = 0 \end{aligned} \tag{19}$$

- Assuming perfect bounding, at the interface between the layer and the substrate $z_1 = l_0$, continuity of the tangential stresses and displacements is required:

$$\begin{aligned} &u^s_1(x, y, 0) = u^c_1(x, y, l_0) \\ &u^s_2(x, y, 0) = u^c_2(x, y, l_0) \\ &u^s_3(x, y, 0) = u^c_3(x, y, l_0) \\ &\sigma^s_{31}(x, y, 0) = \sigma^c_{31}(x, y, l_0) \\ &\sigma^s_{32}(x, y, 0) = \sigma^c_{32}(x, y, l_0) \\ &\sigma^s_{33}(x, y, 0) = \sigma^c_{33}(x, y, l_0) \end{aligned} \tag{20}$$

This completes the governing equations and boundary conditions for the 3D elastic layered contact problem. Various numerical methods exist to solve these 3D equations, e.g. MG methods [4], Fast Fourier Transform (FFT) methods [38,39] and Finite Element Methods (FEM) [42], each with their own merit. In this work, the FFT method has been used, because in the Fourier transform domain the viscoelastic equations are equivalent to the elastic equations for contact problems according to the elastic–viscoelastic correspondence principle [28,43]. The deformation and stress equations in the frequency domain are as follows.

Fourier transform of the Papkovich–Neuber potentials ϕ and ψ_i $(i = 1, 2, 3)$ with respect to x and y gives:

$$\begin{aligned} \tilde{\phi}^k &= A^k e^{-\alpha z_k} + \bar{A}^k e^{\alpha z_k} \\ \tilde{\psi}^k_1 &= B^k e^{-\alpha z_k} + \bar{B}^k e^{\alpha z_k} \\ \tilde{\psi}^k_3 &= C^k e^{-\alpha z_k} + \bar{C}^k e^{\alpha z_k} \end{aligned} \tag{21}$$

where the symbol $\approx$ indicates double Fourier transform in x and y, and $\alpha = \sqrt{m^2 + n^2}$ with m and n being the Fourier transform variables corresponding to x and y, respectively. Note that ψ_2 vanishes when body forces are ignored [44]. Based on the linear elasticity assumption, the deformation and stress components in Eq. (18) can be represented in the Fourier domain as

$$\begin{aligned} \tilde{\tilde{u}}^k_i &= \frac{1}{2\mu^k}\left[\tilde{\tilde{\psi}}^k_{,i} + FT_{xy}(x\psi^k_{1,i}) + z\tilde{\tilde{\psi}}^k_{3,i} - \left(3 - 4\nu^k\right)\tilde{\tilde{\psi}}^k_i\right] \\ \tilde{\tilde{\sigma}}^k_{ij} &= \tilde{\tilde{\phi}}^k_{,ij} - 2\nu^k(\tilde{\tilde{\psi}}^k_{1,1} + \tilde{\tilde{\psi}}^k_{3,3})\delta_{ij} - (1-2\nu^k)(\tilde{\tilde{\psi}}^k_{i,j} + \psi^k_{j,i}) + FT_{xy}(x\psi^k_{1,ij}) + z\tilde{\tilde{\psi}}^k_{3,ij} \end{aligned} \tag{22}$$

where FT_{xy} indicates the double Fourier transform with respect to x and y. The detailed expression of Eq. (22) of all displacement and stress components are given in Appendix C. Eq. (21) shows that 12 unknown coefficients A^k, B^k, C^k, $\bar{A}^k$, $\bar{B}^k$ and $\bar{C}^k$ with $k = c$ or $k = s$ need to be determined in order to solve the problem. The condition that the displacements and stresses should vanish at infinity in z direction of the substrate leads to $\bar{A}^s = \bar{B}^s = \bar{C}^s = 0$. The remaining nine unknown coefficients can be solved from the nine boundary conditions, as given in Eqs. (19) and (20). The detailed expressions are given in Appendix C.

4.2. Correspondence principle and viscoelastic layered solution

Green's functions are the solution of the potential response of the studied system when subjected to a unit force. It is also referred as influence coefficient and has been widely used to calculate the deformation of an elastic half-space. According to the elastic–viscoelastic correspondence principle, the Green's function for a viscoelastic half-space can be obtained from the corresponding elastic one. The analysis and the derivation process are given in Appendix D for point contact

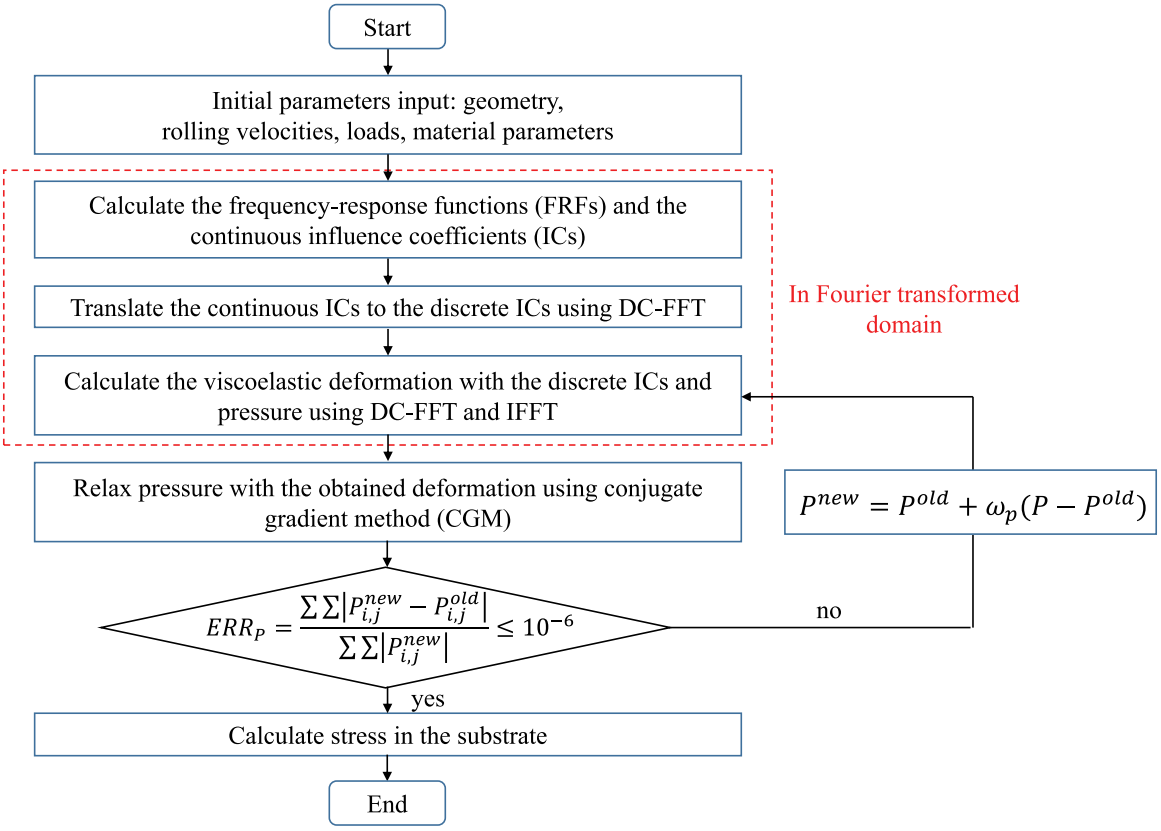

Fig. 4. Flow chart of the Navier–Cauchy equations based potential model for viscoelastic layered contact problem. The DC-FFT algorithm is used for the surface deformation and material stress calculations.

problems. The main points for homogeneous half-space are summarized as:

(1) In the spatial domain: the time-dependent viscoelastic Green's function can be derived from the elastic Green's function by replacing the compliance, $1/E$, with the compliance function of the viscoelastic model, $\varphi_c(t)$.
(2) In the Fourier domain: the steady-state viscoelastic Green's function can be directly obtained from the transformed elastic Green's function by replacing the elastic modulus E with the relaxation function $\psi_r(\omega)$.

For describing the deformation of elastic layered contact problems, the Green's function is not available in the spatial domain, but it does exist in the frequency domain. Liu et al. [45] and Wang et al. [38,39] proposed that the stress and displacement components given by Eq. (22) can be regarded as the transform of the Green's functions referred as the Frequency Response Functions (FRFs) obtained from a Dirac delta function as the pressure excitation in Eq. (19). Hence, the transformed viscoelastic Green's functions or FRFs in steady-state can be obtained by replacing the elastic modulus $\frac{1}{2\mu^k}$ in Eq. (22) with the relaxation function of the viscoelastic model $\hat{\psi}_r^k(\omega)$.

For the present layered contact under frictionless rolling conditions, the FRF of normal displacement of the viscoelastic layer can be derived from Eq. (C.3)

$$\tilde{\tilde{u}}_3^c(m,n,\omega) = \hat{\psi}_r^c(\omega)\left\{-\alpha(A^c e^{-\alpha z^c} - \bar{A}^c e^{\alpha z^c}) - (3-4\nu^c)(C^c e^{-\alpha z^c} + \bar{C}^c e^{\alpha z^c}) - \alpha z^c (C^c e^{-\alpha z^c} - \bar{C}^c e^{\alpha z^c})\right\} \tag{23}$$

The obtained transformed elastic/viscoelastic Green's functions (FRFs) are used to calculate the continuous Fourier transform Influence Coefficients (ICs), $\tilde{\tilde{C}}_{sub}^{sup}$ with the subscript representing the excitation, and the superscript indicating the response. For example, the influence coefficient linking the pressure excitation p and the normal displacement u_3^c of the viscoelastic layer is

$$\tilde{\tilde{C}}_p^{u_3^c}(m,n,\omega) = \tilde{\tilde{u}}_3^c(m,n,\omega)\tilde{\tilde{Y}}(m,n) \tag{24}$$

where $\tilde{\tilde{u}}_3^c$ is the viscoelastic FRF given by Eq. (23) and $\tilde{\tilde{Y}}$ is the Fourier transformed shape function [38]. A discrete convolution and fast Fourier transform (DC-FFT) algorithm can be used to translate the continuous $\tilde{\tilde{C}}$ to the discrete forms $\hat{\tilde{C}}$ to account for arbitrary pressure shape at the top boundary in Eq. (19). For the procedure of this translation from $\tilde{\tilde{C}}$ to $\hat{\tilde{C}}$ and the shape function, see [38,39].

By applying the Inverse Fast Fourier Transform (IFFT) and linking the time-related frequency variable ω to rolling velocity v_m and the space-related frequency variable m by the relation $\omega = mv_m$, the steady-state response of the normal displacement is obtained

$$u_3^c(x,y) = IFFT\left[\hat{\tilde{C}}_p^{u_3^c}(m,n,mv_m)\cdot\hat{\tilde{p}}(m,n)\right] \tag{25}$$

For details of the derivation of Eq. (25), interested readers are referred to [28]. By substituting $u_3^c(x,y)$ in the gap height equation Eq. (4), the problem can be fully solved by coupling the stresses and displacements with the governing equations. Correspondingly, in a steady-state regime, the layer thickness after deformation is

$$l(x,y) = l_0 + u_3^s(x,y) - u_3^c(x,y) \tag{26}$$

In the literature, the 3D contact problem of an elastic layer perfectly bonded to an elastic substrate has first been solved by O'Sullivan and King [46] with the FFT method in 1988. Based on this work, Wang et al. [38,39] extended the solution to imperfectly bonded interfaces between the elastic layer and the substrate, e.g. dislocation-like and

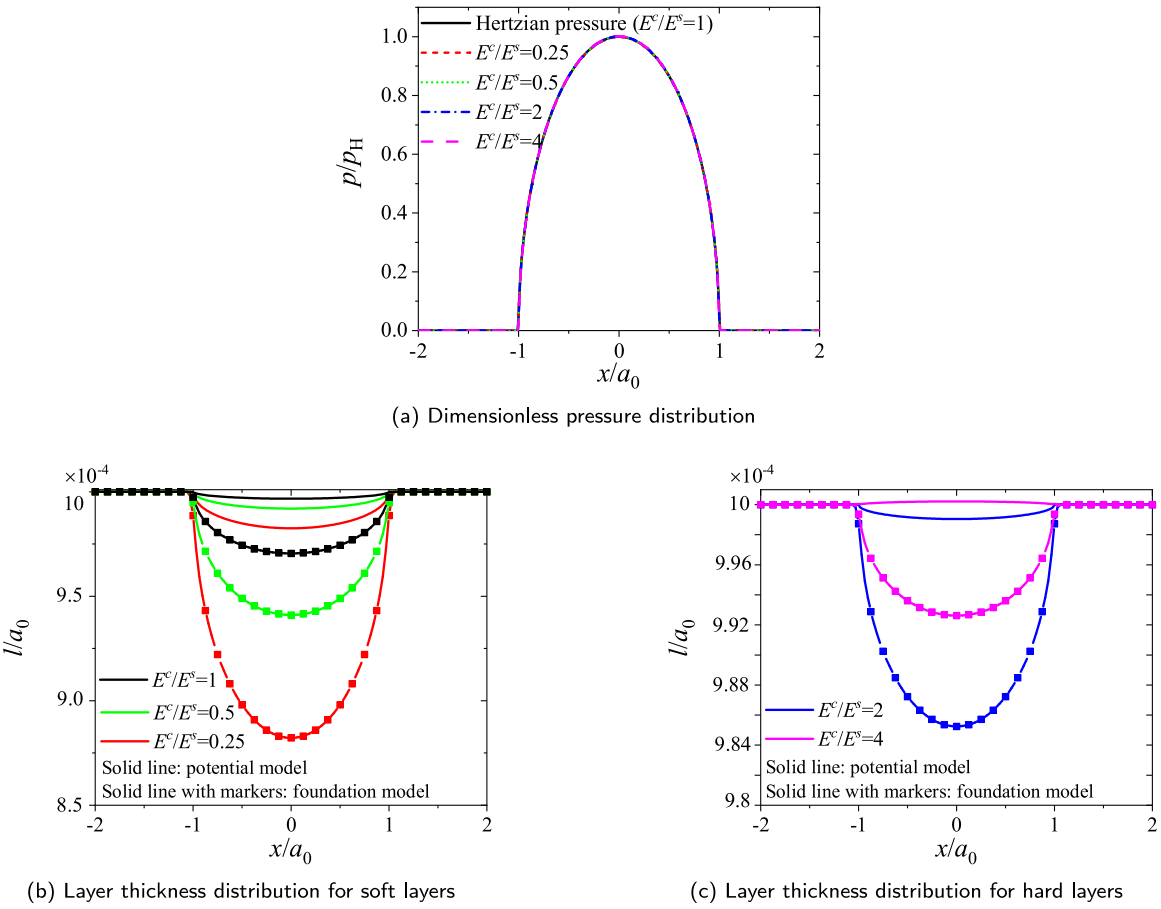

Fig. 5. Comparison of pressure and deformed layer thickness profile between the potential model and the foundation model for thin elastic layer coated elastic substrate at different coating stiffness by varying E^c/E^s. (a) Dimensionless pressure, and layer thickness profiles along the central line for a thin (b) soft or (c) hard elastic layer at thickness l_0/a_0. The pressure remains the same for the two models, then only the results obtained with the potential model are presented in (a).

force-like interface discontinuities. More recently, Zhang et al. [28] extended the elastic layered model to a viscoelastic model.

In the present study, the models proposed in [37–39] are taken as reference to investigate the thin viscoelastic layer behavior in rolling contacts. A schematic overview of the different steps in the solution of the problem is given in Fig. 4. The main difference lies in the layer deformation calculation, in which the modulus of the elastic layer needs to be replaced by the relaxation function of the viscoelastic model. Taking the Hertzian contact radius a_0 and the maximum pressure p_H given in Eq. (12) as the dimensionless parameters, the dimensionless form of the steady-state relaxation function in the frequency domain can be obtained from Eq. (3) by setting $\omega = mv_m$, resulting in:

$$\bar{\tilde{\psi}}_r(\bar{m}v_m) = 1/\left[\frac{1}{\bar{E}^c_\infty} + \left(\frac{1}{\bar{E}^c_0} - \frac{1}{\bar{E}^c_\infty}\right)\frac{1}{1+i\bar{m}De}\right] \tag{27}$$

where the symbol – represents the dimensionless form, $De = v_m\tau/a_0$ and $\bar{m}$ is the dimensionless frequency variable corresponding to the variable $X(= x/a_0)$ in the spatial domain.

The pressure distribution is solved with a computational domain of $(-8a_0, 4a_0)$ and $(-4a_0, 4a_0)$ with 513*513 grid points in the x and y direction, respectively. A relative convergence criteria is used regarding the calculated pressures,

$$ERR_P = \sum\sum\left|P^{new}_{i,j} - P^{old}_{i,j}\right| / \sum\sum\left|P^{new}_{i,j}\right| \le 10^{-6} \tag{28}$$

In the subsequent stress calculations, there are 80 equidistant grid points in the layer in z direction.

5. Results and discussion

In literature, the output of viscoelastic layered contact problems mainly consist of the pressure distribution, the stress field and the total deformation. As a contrast, the layer thickness after deformation rarely gains attention. To investigate the possibility of using a thin viscoelastic layer to represent EHL film behavior, the layer thickness after deformation is a key parameter. To ensure that the thickness of the layer is comparable to an EHL film, the un-deformed layer thickness relative to the contact radius is taken as $l_0/a_0 = 10^{-3}$ in the following analysis. The Poisson ratio is taken as 0.3 for both the layer and the substrate, i.e. $\nu^c = \nu^s = 0.3$. The Hertzian parameters calculated with the mechanical properties of the substrate, a_0 and p_H in Eq. (12), are used for the non-dimensionalization of the layer thicknesses and stresses, respectively.

In Appendix A, the potential solution has been verified thoroughly by comparing the simulation results with the ones in literature for various contact problems, such as elastic and viscoelastic layered elastic substrate contact, viscoelastic half-space contact. It serves as a reference to investigate the effectiveness of the foundation approach as well as the two assumptions used. In Section 5.1, the simulation results with the foundation approach are compared with the verified potential

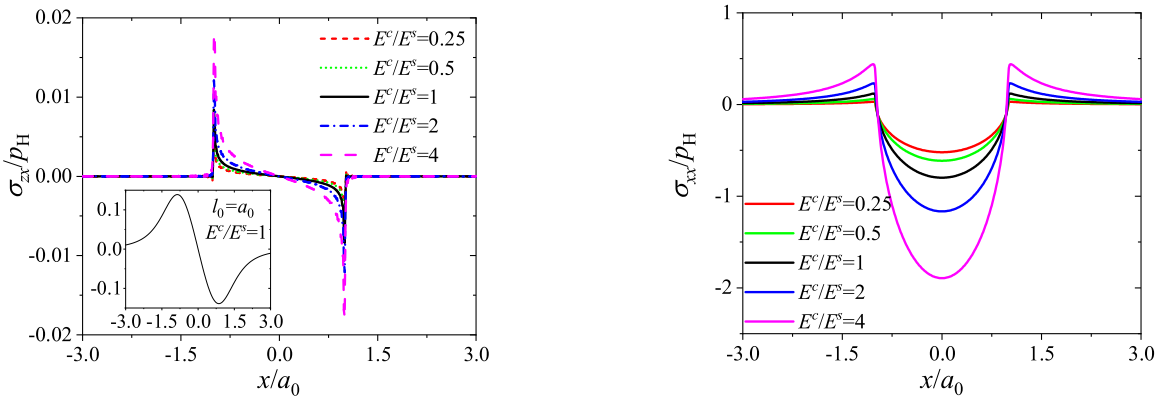

(a) Dimensionless layer/substrate interface stress σ_{zx} (b) Dimensionless layer/substrate interface stress σ_{xx}

Fig. 6. Dimensionless stress components (a) σ_{zx}, (b) σ_{xx} at the layer/substrate interface for different values of E^s/E^c in elastic layered contacts.

solution firstly. Subsequently, a parametric study is carried out with the potential solution in Section 5.2 to have a comprehensive understanding of the viscoelastic layered contact problem. Finally, the possibility of modeling the EHL film behavior through the concept of viscoelastic layer is explored in Section 5.3.

5.1. Foundation model vs potential model

In this section, the comparison of the two solutions is performed first for elastic layered contact problems in Section 5.1.1 and then for viscoelastic layered ones in Section 5.1.2.

5.1.1. Elastic layered elastic half-space

With the developed potential solution, an elastic layered solution can be obtained simply by setting $E^c_\infty = E^c_0$ in the SLS model so that the resulting elastic modulus of the layer is $E^c = E^c_0$. The response of an elastic layered contact problem is dominated by two dimensionless parameters, the relative layer thickness l_0/a_0 and the relative layer stiffness E^c/E^s (the ratio of the elastic modulus of the layer relative to the substrate). In this section, the effect of the relative layer stiffness E^c/E^s is studied at a constant layer thickness of $l_0/a_0 = 0.001$. The input values for E^c/E^s are the same as used in [46] or in Appendix A.1. They are achieved by fixing the elastic modulus E^s of the substrate and varying E^c. Note that for elastic layered contact problems, the dynamic rolling cases and the static case share the same deformation and pressure distribution.

Fig. 5 shows the pressure profile and the deformed layer thickness at different elasticity ratios E^c/E^s. When $E^c/E^s = 1$, the layered elastic contact problem returns to an elastic half-space (Hertzian contact problem), which serves as a reference for other cases of $E^c/E^s < 1$ (soft compliant layer) and $E^c/E^s > 1$ (hard stiff layer). For such a thin layer, it can be seen in Fig. 5(a) that the pressure distribution remains the same for all cases, that is, being the same as the elastic half-space solution (Hertzian pressure) regardless of the elastic modulus ratios. A similar phenomenon has also been reported by Chen [47] and O'sullivan [46]. The layer thickness given in Fig. 5(b) shows that the more compliant layer with a smaller elasticity ratio E^c/E^s has a larger deformation. For the stiffest layer of $E^c/E^s = 4$ in Fig. 5(c) used in this study, the deformed layer thickness is even larger than its initial value. In this case, the stiffer layer behaves as a beam attached to the elastic half-space resulting in bending stresses in the layer [46,47], which causes the increase in its thickness. Fig. 5(b) and (c) shows that the foundation model predicts larger layer deformation than the potential model for both soft and hard layer cases. In addition, the foundation model cannot predict the bending effect for the hard layer case $E^c/E^s = 4$ as a result of the oedometric layer assumption. Note that in all cases the deformation of the substrate is many times larger than the thickness of the layer.

The interfacial stresses, σ_{zx} and σ_{xx}, at $z_1 = l_0$, are plotted in Fig. 6 for different layer stiffness calculated with the potential solution. The profiles of σ_{zx} in Fig. 6(a) show that a compression zone occurs in front of the rolling contact and a traction zone behind. The interfacial shear stress becomes larger when the elastic modulus of the layer increases relative to the substrate. Compared to the relative thick layer of $l_0 = a_0$ in the inset in Fig. 6(a), the thin layer causes the shear stresses σ_{zx} to concentrate at the edges of the contact zone with a local maximum. For this thin layer case of $l_0 = 0.001a_0$, the curves of σ_{xx} in Fig. 6(b) show that the stiffer layer further increases both the maximum tensile and compressive stresses at the interface. The rate of increase is becoming larger with increasing elasticity ratios.

To have an overall representation of the stresses, the corresponding dimensionless von Mises stresses (the second invariant of the stress deviator tensor) are calculated according to Eq. (29)

$$\sigma_{VM} = \sqrt{\frac{1}{2}\left[(\sigma_{xx}-\sigma_{yy})^2 + (\sigma_{yy}-\sigma_{zz})^2 + (\sigma_{zz}-\sigma_{xx})^2 + 6(\sigma_{xy}^2 + \sigma_{xz}^2 + \sigma_{yz}^2)\right]} \tag{29}$$

The result obtained with the potential solution is presented in a cross sectional view of the central plane $y = 0$. The elastic case of $E^c/E^s = 1$ in Fig. 7 is exactly a regular homogeneous contact with the maximum stress of $0.62p_H$ at a depth measured downwards approximately $0.47a_0$ below the surface as reported in [4]. The von Mises stress fields in the elastic substrate remain almost the same for all cases as shown in Fig. 8. However, significant discontinuities occur at the interface between the layer and the substrate for all cases. The extent of discontinuity increases when the layer becomes either harder or softer. For the soft compliant layer in Fig. 8(a) and (b), the von Mises stress concentrates in the Hertzian zone, spanning roughly from −1 to 1 in the x direction and increases mainly in the center of the contact. As a contrast, the hard stiffer layer in Fig. 8(d) and (e) has a wider stress distribution area, and the von Mises stress in the film first concentrates on the edge of the contact area and then increases inside the contact zone with increasing elastic modulus.

As a short summary, the ratio E^c/E^s has a strong effect on the layer deformation and the stress discontinuities at the layer/substrate interface. However, it has negligible influence on the pressure response

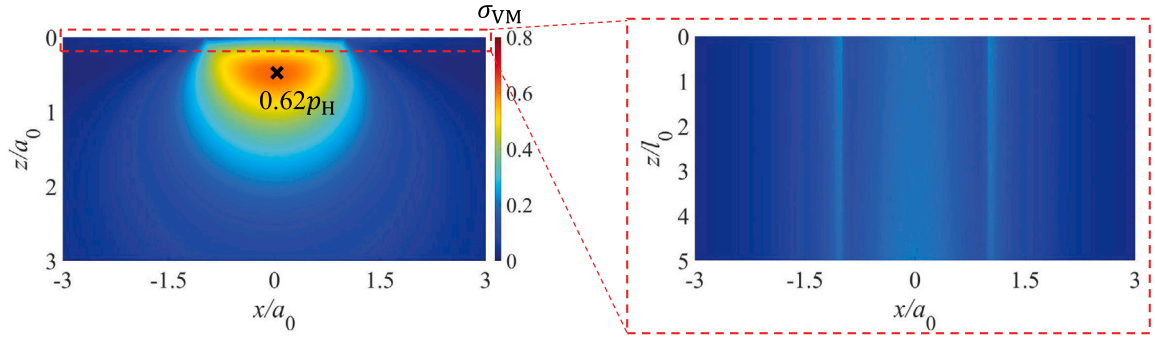

Fig. 7. Dimensionless von Mises stress field on plane $y = 0$ for a homogeneous elastic half-space $E^s/E^c = 1$.

of the elastic layer-elastic substrate system when the layer thickness is much smaller than the contact radius $l_0 \ll a_0$. In such cases, the substrate dominates the pressure distribution.

5.1.2. Viscoelastic layered elastic half-space

In this section, the pressure distribution and the deformed layer thickness predicted by the two approaches are compared for a viscoelastic layered rolling contact (elastic substrate) at different speeds. The common input parameters are: a sphere radius $R_0 = 9.525$ mm, an applied load $W_0 = 10$ N, substrate elastic modulus $E^s = 1$ GPa, Poisson ratio $\nu^c = \nu^s = 0.3$, and for the viscoelastic layer a modulus $E_0^c = 0.1$ GPa with a ratio $E_\infty^c/E_0^c = 10$. In this case, the layer thickness is as thin as $l_0 = 1 \times 10^{-3} a_0$, which is in the range of an EHL film.

Fig. 9 compares the dimensionless pressure distribution (a) and the layer thickness (b) calculated from the two approaches at different values of De, $0.01 \le De \le 10$, corresponding to rolling speeds from 4×10^{-4} to 0.4 m/s when the relaxation time of the layer is $\tau = 0.01$ s. The pressure distribution is identical to the Hertzian profile associated with the substrate elastic modulus for all cases. The effect of the viscoelastic layer on the pressure distribution is negligible. This phenomenon is similar to the elastic layered contact problems as studied in the last section.

For the layer thickness profiles in Fig. 9(b), the results from the foundation model show similar trends of variation compared to the results from the potential model, even though quantitatively the resulting layer thickness is smaller for the former. This is caused by the oedometric layer assumption used in the foundation approach, which neglects the compatibility relation of deformation with the surrounding non-local points. This leads to a larger deformation in the normal direction and hence a smaller layer thickness. The results imply that the relatively simple foundation model can predict the layer deformation behavior qualitatively quite well even though it is not as accurate as the potential model.

5.2. Parameter study with potential solution

Compared to the elastic layered contact problem in the previous Section 5.1.1, the viscoelastic layer-elastic substrate system introduces two additional dimensionless parameters: E_∞^c/E_0^c the ratio of the two elastic limits of the SLS viscoelastic layer, and the Deborah number De which relates the relaxation time of the viscoelastic material τ to the characteristic time of the material passing through the contact a_0/v_m. As a result, the studied viscoelastic layered contact problem with a specific layer thickness l_0/a_0 is governed by three dimensionless parameters: (1) the ratio of the elastic modulus E_∞^c/E^s, (2) the dimensionless velocity or the Deborah number $De = v_m\tau/a_0$, and (3) the ratio of the two elastic limits of the SLS model $E_\infty^c/E_0^c = 1 + R_e$. In this section, the influence of these parameters on the contact pressure distribution and the deformed layer thickness is investigated under thin-layer rolling contact conditions.

5.2.1. Effect of the ratio of elastic modulus, E_∞^c/E^s

The effect of the elastic modulus ratio E_∞^c/E^s on the pressure distribution, layer deformation and subsurface stresses is investigated in the thin layer regime of $l_0 = 0.001a_0$. As before, the elastic modulus of the elastic substrate E^s is fixed and the layer modulus E_∞^c is varied to achieve different ratios of E_∞^c/E^s. The Deborah number De and the ratio of the two elastic modulus of the SLS model E_∞^c/E_0^c are prescribed as 0.8 and 10, respectively.

Fig. 10(a) and (b) show the centerline dimensionless pressure distribution and the layer thickness after deformation, respectively, for different ratios of E_∞^c/E^s from 0.25 to 4. Similar to the elastic solution that has been shown in Fig. 5(a), the pressure profiles in Fig. 10(a) are all nearly identical to the classical Hertzian analytical result, but are quite different from the case for a thick viscoelastic layer of $l_0 = a_0$ shown in Fig. A.3. This is the consequence of the studied very thin layer. The pressure does not vary much over the layer thickness; hence, it is dominated by the substrate. Fig. 10(b) shows that a more compliant layer (with smaller elastic modulus ratio E_∞^c/E^s) has a larger layer deformation. The solid black line in the figure represents the solution of an elastic layered half-space and serves as a reference to the rest. Symmetric layer thickness distribution is seen for the elastic layered case, while asymmetric ones are observed for all the viscoelastic layered cases. The asymmetric layer deformation is caused by the time-delayed response of the viscoelastic material and it takes time for a viscoelastic layer to return to its original state at the outlet side, see the left-hand side of Fig. 10(b).

Fig. 11 shows the interfacial stress σ_{xx} and the von Mises stress σ_{VM} at the interface for different elasticity ratios E_∞^c/E^s. In Fig. 11(a), the maximum tensile stress at the outlet side of the contact edge is reduced when the layer is more compliant than the substrate. Compared to the elastic layered solution (black line), the interfacial stress component σ_{xx} is asymmetric and inclined towards the inlet side. For the soft layer cases, $E_\infty^c/E^s = 0.25$ and $E_\infty^c/E^s = 0.5$, there are only slight differences in the profiles of σ_{xx} in the interface. For the hard layer case of $E_\infty^c/E^s = 4$, a local minimum occurs on the inlet side for the interfacial stress σ_{xx}, while for the von Mises stress in Fig. 11(b), it skews to the outlet side and a local maximum appears at the outlet side and fluctuations occur at the inlet side.

5.2.2. Effect of the deborah number, De

This section studies the influence of the Deborah number $De = v_m\tau/a_0$, while keeping the other parameters constant: $E_\infty^c/E^s = 0.25$ and $E_\infty^c/E_0^c = 10$. Fig. 12 shows the centerline pressure (a) and the deformed layer thickness (b) profiles for different dimensionless rolling velocities De of 0.2, 0.4, 0.8 and 1.2. As shown in Fig. 12(a), the pressure distribution at different values of De coincides with the elastic Hertzian pressure because of the thin layer thickness, $l_0 = 0.001a_0$. For the deformed layer thickness shown in Fig. 12(b), the viscoelastic property of the layer results in an asymmetric layer profile for all cases. When the velocity is high (large De) the viscoelastic layer has

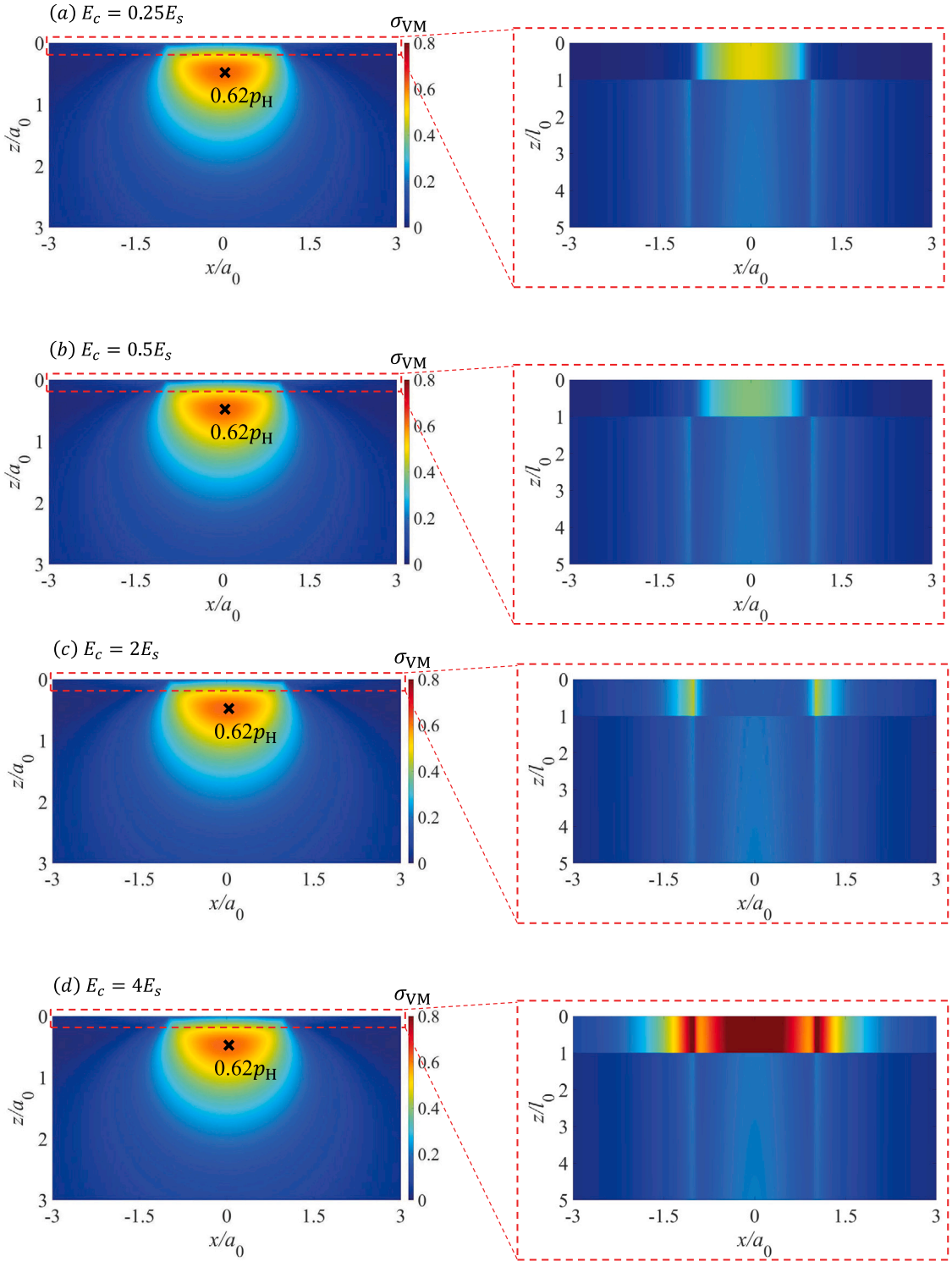

Fig. 8. Dimensionless von Mises stress field on the plane $y = 0$ for elastic layered contacts with different E^s/E^c. (The layer thickness is $l_0 = 0.001a_0$.)

less time to deform resulting in a larger thickness. The results show that the relatively simple foundation predicts the layer deformation behavior qualitatively well, but also that this model is most suited for soft layers with very limited "local support". For more "solid" layers, where 2D/3D effects are important, bending effects lead to a smaller deformation and in cases even to a thickening effect in the center of the contact. These effects can only be modeled with the full model.

The phenomena observed in the results are in line with the behavior of EHL films in classical (starved) lubrication conditions, i.e. limited lubricant supply, high loads, and or low speeds, where the film thickness itself is small, the pressure nearly Hertzian, and the inlet and outlet region, where the transition to fluid flow effects represented by the pressure flow terms in the Reynolds equation takes place, is also very narrow. Classic phenomena related to those terms, i.e. the

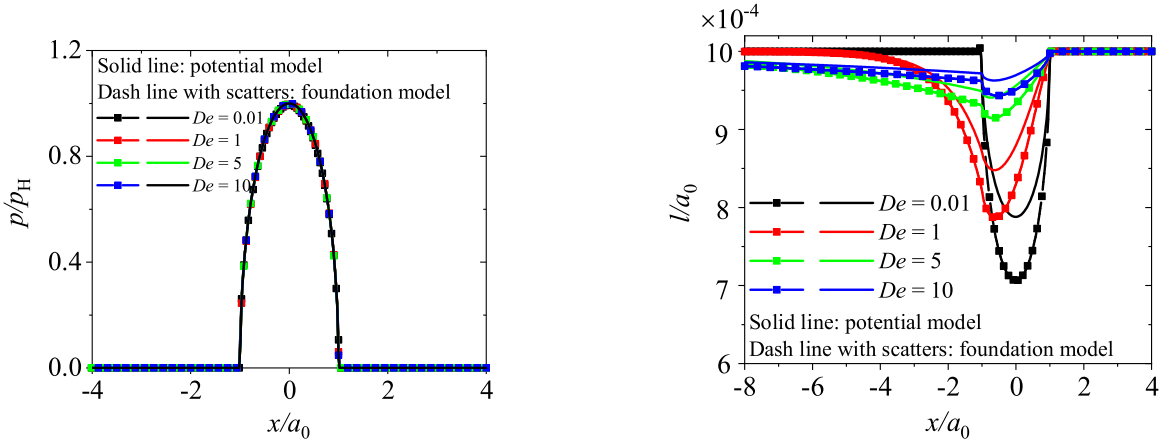

(a) Dimensionless centerline pressure distribution (b) Dimensionless centerline deformed layer thickness

Fig. 9. Comparison of (a) pressure distribution and (b) deformed layer thickness profile along the central line between the potential model and the foundation model for thin viscoelastic layered elastic substrate at different rolling velocities. ($l_0 = 1 \times 10^{-3} a_0$, $E^c_\infty / E^c_0 = 10$ and $E^s / E^c_0 = 10$. The right side is the rolling entrance.)

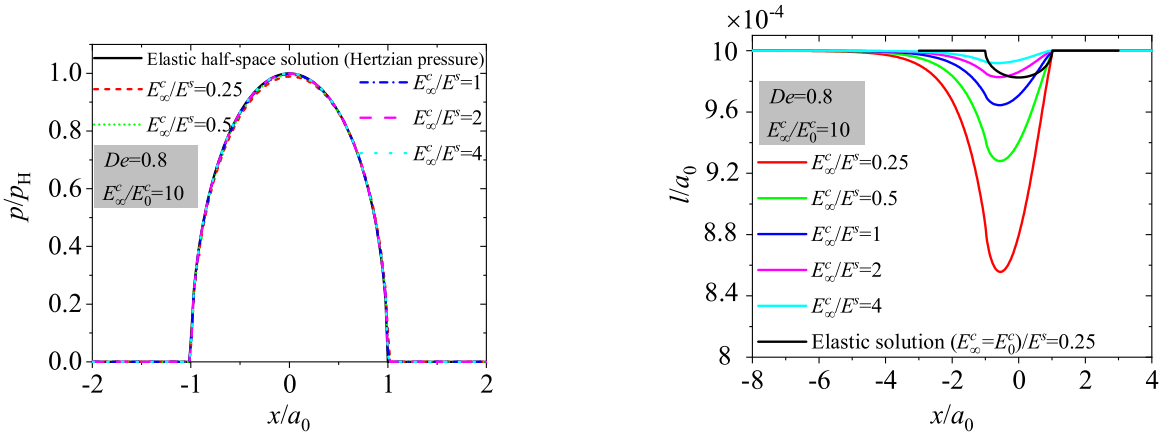

(a) Dimensionless pressure distribution (b) Dimensionless layer thickness

Fig. 10. Centerline profiles of pressure distribution (a) and layer thickness after deformation (b) for different values of E^c_∞ / E^s in viscoelastic layered contacts. (SLS viscoelastic model with $E^c_\infty / E^c_0 = 10$ at a fixed viscoelastic layer thickness of $l_0 = 0.001 a_0$ and $De = 0.8$; the right side is the rolling entrance.)

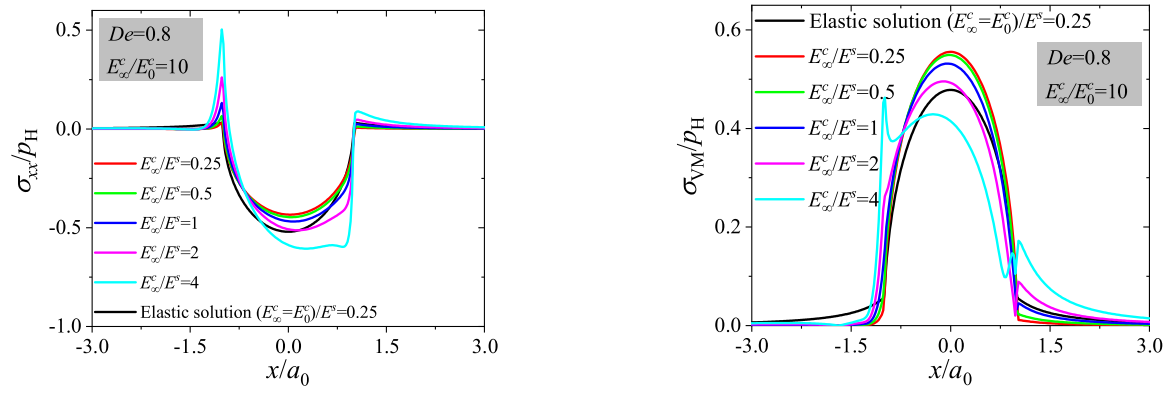

(a) Dimensionless layer/substrate interface stress σ_{xx} (b) Dimensionless von Mises stress σ_{VM}

Fig. 11. Dimensionless layer/substrate interface stress (a) σ_{xx}, and the corresponding von Mises stress (b) σ_{VM} for different elasticity ratios E^c_∞ / E^s in viscoelastic layered contacts. (SLS viscoelastic model with $E^c_\infty / E^c_0 = 10$, at a fixed viscoelastic layer thickness of $l_0 = 0.001 a_0$ and $De = 0.8$; the right side is the rolling entrance.)

"inlet pressure sweep", and the out of contact flow causing the film constriction at the sides (horse-shoe) and the outlet region, are not seen. These cannot be mimicked with uniform layer properties.

The layer/substrate interfacial stresses are plotted in Fig. 13. The elastic layered solution is given in the figure by the black solid line as a reference. The central line profiles of σ_{xx} in Fig. 13(a) show that the viscoelasticity of the layer induces smaller stress values than the

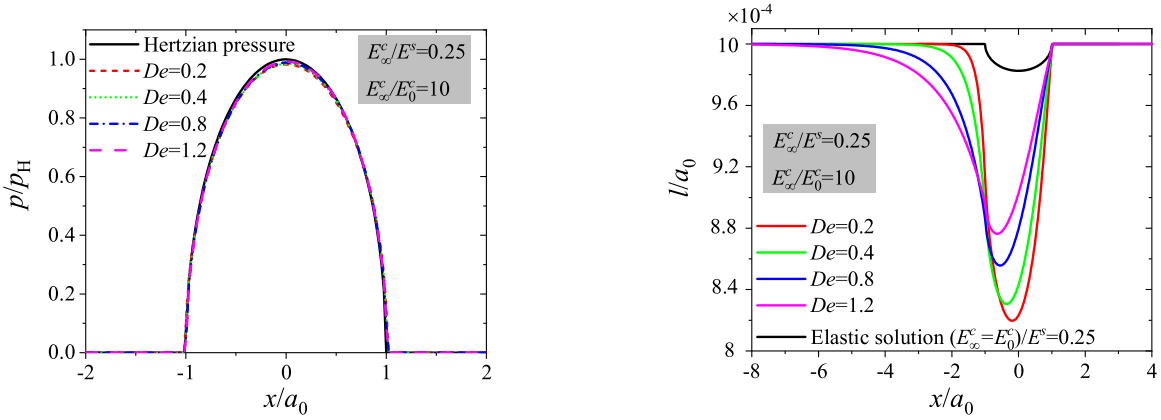

Fig. 12. Centerline profiles of pressure distribution (a) and layer thickness after deformation (b) for different values of speed De in viscoelastic layered contacts. (SLS viscoelastic model with $E^c_\infty/E^c_0 = 10$, at fixed values of $l_0 = 0.001a_0$ and $E^c_\infty/E_s = 0.25$; the right side is the rolling entrance.)

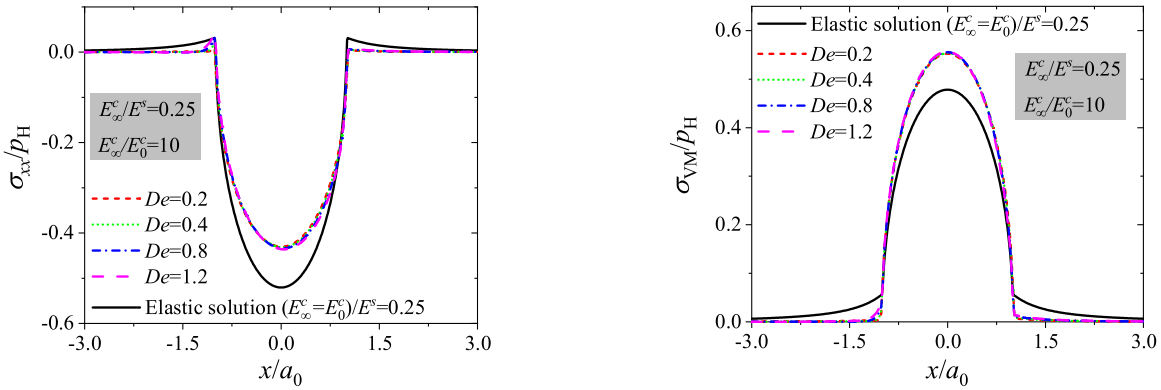

Fig. 13. Dimensionless layer/substrate interface stress (a) σ_{xx}, and the corresponding von Mises stress (b) σ_{VM} for different speeds De in viscoelastic layered contacts. (SLS viscoelastic model with $E^c_\infty/E^c_0 = 10$, at fixed values of $l_0 = 0.001a_0$ and $E^c_\infty/E_s = 0.25$; the right side is the rolling entrance.)

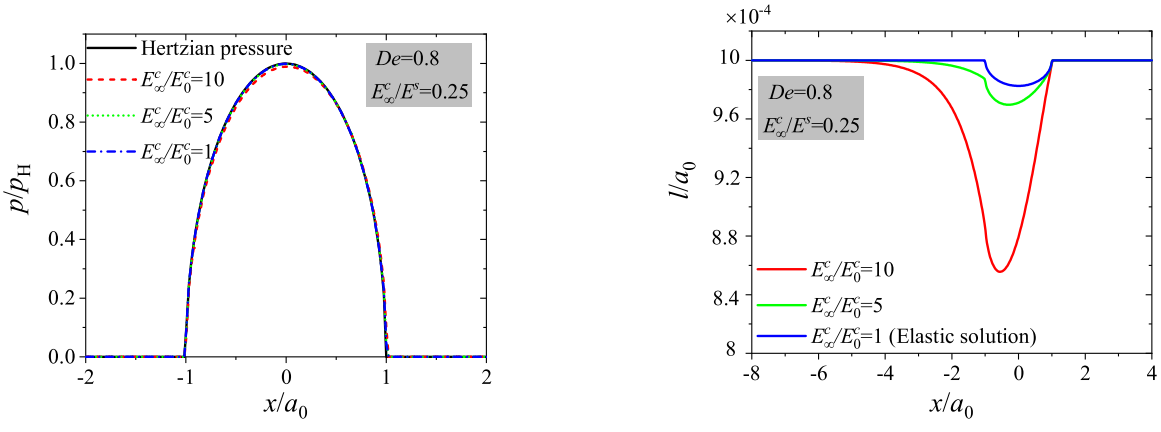

Fig. 14. Centerline profiles of pressure distribution (a) and layer thickness after deformation (b) for different values of E^c_∞/E^c_0 in viscoelastic layered contacts. (SLS viscoelastic model with a single relaxation time, at fixed values of $l_0 = 0.001a_0$ and $De = 0.8$; the right side is the rolling entrance.)

elastic one, while the increase in the rolling velocity from 0.2 to 1.2 causes almost no change to σ_{xx}. Regarding the von Mises stresses at the layer/substrate interface in Fig. 13(b), an increase is observed for the viscoelastic case compared to the elastic solution. The central line profiles of the von Mises stress σ_{VM} show a smaller sweep zone at both the inlet and outlet sides compared to the elastic case. Nevertheless, the

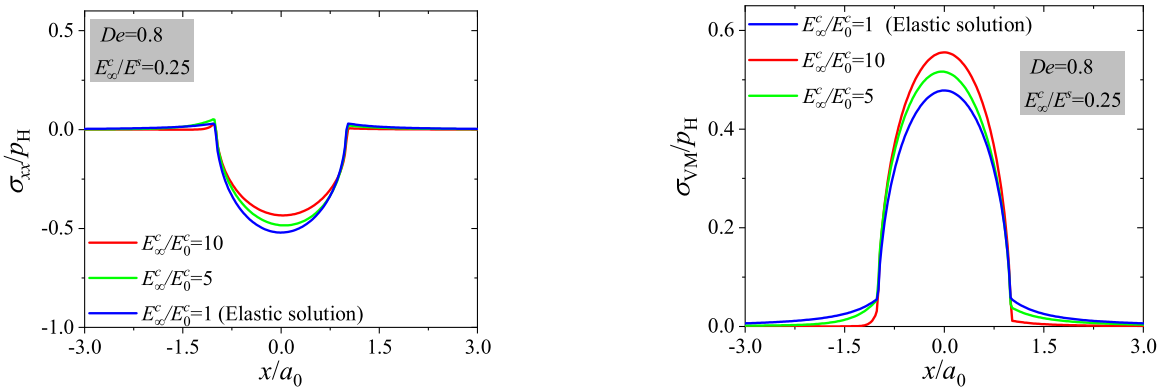

(a) Dimensionless stress σ_{xx} (b) Dimensionless von Mises stress σ_{VM}

Fig. 15. Dimensionless layer/substrate interface stress (a) σ_{xx}, and the corresponding Von Mises stress (b) σ_{VM} for different ratio values of E^c_∞/E^c_0 in viscoelastic layered contacts. (SLS viscoelastic model with a single relaxation time, at fixed values of $l_0 = 0.001a_0$ and $De = 0.8$; the right side is the rolling entrance.)

values of the von Mises stresses remain similar to each other for all the studied viscoelastic cases with the set of speeds applied at frictionless and thin layer conditions.

5.2.3. Effect of the ratio of the two elastic limits of the SLS model, E^c_∞/E^c_0

In this section, the effect of the ratio of the two elastic limits in the SLS model for the viscoelastic layer, E^c_∞/E^c_0, is studied. These two elastic limits correspond to the rubbery state and the glassy state of viscoelastic materials at extremely low and high frequencies, respectively, as shown in Fig. B.1. We keep the other parameters constant: $l_0 = 0.001a_0$, $De = 0.8$ and $E^c_\infty/E^s = 0.25$.

Fig. 14 shows the dimensionless pressure distribution and the deformed layer thickness for various ratios of $E^c_\infty/E^c_0 = 1$, 5 and 10. For $E^c_\infty/E^c_0 = 1$, the viscoelastic layered solution reduces to the elastic layered solution, according to Eq. (3). Note that $E^c_\infty/E^c_0 = (1 + R_e)$ cannot be smaller than one as $R_e = E_f/E_s \geq 0$. The plots in Fig. 14(a) show that the effect of the ratio of the two elastic limits of the SLS model on the pressure distributions is negligible for the studied thin layer regime, while it has considerable effect on the layer deformation as shown in Fig. 15(b). The layer with a larger E^c_∞/E^c_0 possesses a larger layer deformation.

Fig. 15 shows the corresponding dimensionless stresses, i.e. the σ_{xx} and the von Mises stress σ_{VM}, at the layer/substrate interface. The viscoelasticity of the layer causes the stress distribution to be slightly skewed to the inlet side for all cases. The hard layer, e.g. $E^c_\infty/E^c_0 = 5$ or $E^c_\infty/E^c_0 = 10$, gives larger σ_{xx} and smaller von Mises stress σ_{VM} compared to the elastic layered case of $E^c_\infty/E^c_0 = 1$.

From the above analysis in Section 5.2, it can be seen that the properties of the elastic substrate dominate the pressure response of the system in the thin layer regime so that an elastic Hertzian pressure distribution remains for all the studied cases. We may say that the pressure distribution of the viscoelastic layered dry contacts is similar to that of the classical EHL in particular at high contact pressures. However, the variation of the dimensionless parameters has significant effect on the layer deformation and the stress components at the layer/substrate interface.

The viscoelasticity of the layer leads to the asymmetric deformation of the system, since it needs time for the layer to recover to its original status resulting in a larger unrecovered deformation at the outlet. However, the deformed layer in contacts is hard to show the EHL film behavior, such as lack of the rather flat parallel film in the middle contact and the film constriction near the outlet. This may attribute to the constant viscosity and thus the constant relaxation time used in the SLS model for the viscoelastic layer. At high Hertzian contact pressure in the order of GPa, the viscosity of the viscoelastic layer and thus the relaxation time in the SLS model might increase significantly. If so, however, this is beyond the scope of the linear viscoelasticity theory and brings new challenges to full-system modeling and numerical simulations. As a first attempt, the effect of the pressure-dependent viscosity on the deformation of the thin viscoelastic layer is studied in a simple manner with the foundation (Winkler) model in the following section.

5.3. Towards EHL film behavior modeling

In the previous section it has been shown that fully bonded viscoelastic layer with isotropic homogeneous behavior do not show typical EHL characteristics in contacts. Here we resort to the foundation model, which may provide an easier framework to consider the piezoviscous effect of the thin viscoelastic layer, even though it is out of the scope of linear viscoelasticity.

As a preliminary study, the pressure-viscosity relation proposed by Roelands, among others, is adopted to model the viscosity of the dashpot in the SLS layer.

$$\eta_s = \eta_{s0}\exp\left[\left(\ln(\eta_{s0}) + 9.67\right)\left(-1 + (1 + \frac{p}{p_0})^z\right)\right] \tag{30}$$

where η_{s0} is the viscosity of the dashpot at ambient pressure p_0, and z is the pressure viscosity index.

The input parameters for the viscoelastic layered model based on the foundation approach are: a loading force of $W_0 = 10$ N, a sphere radius of $R_0 = 9.525$ mm, a rolling velocity of $v_m = 0.1$ m/s, an SLS viscoelastic layer thickness of $l_0 = 0.001a_0$, modulus of $E^c_0 = 1$ GPa, ratio of $E^c_\infty/E^c_0 = 1000$, layer viscosity of $\eta_{s0} = 44700$ Pa s, pressure constant of $p_0 = 0.196$ GPa, viscosity pressure index of $z = 0.67$, and reduced modulus of a steel–glass contact of $E' = 117$ GPa that is widely used in optical EHL for validation purpose.

Fig. 16 shows the resulting pressure and layer thickness distribution along the central line with the above input parameters. For the pressure distribution, as reported in the last section Section 5.2, it coincides with the Hertzian pressure because of the thin layer thickness and the dominating effect of the elastic substrate. Interestingly, with such easy consideration of the piezoviscous effect of the SLS viscoelastic layer, the deformed layer behaves as an EHL film showing a relatively constant film thickness in the contact center and a local minimum near the exit. Inside the contact zone, the local viscosity and thus the relaxation time of the viscoelastic layer increase depending on the local contact pressure. In the contact center the viscosity becomes extremely large, which delays the deformation of the SLS viscoelastic layer and hence

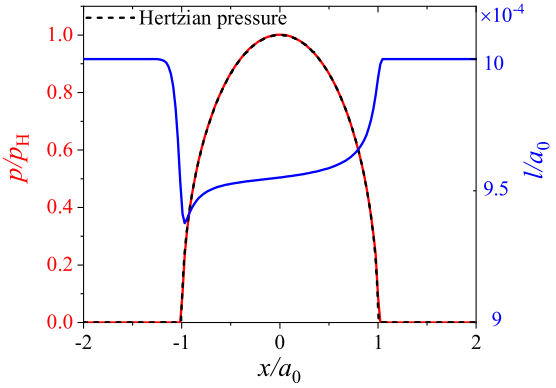

Fig. 16. Pressure and layer thickness distribution along the central line predicted by foundation approach of viscoelastic layer modeling by considering the piezoviscous effect of the dashpot in the SLS model. (v_m = 0.1 m/s, SLS viscoelastic model with $E^c_\infty/E^c_0 = 1000$; the right side is the rolling entrance.)

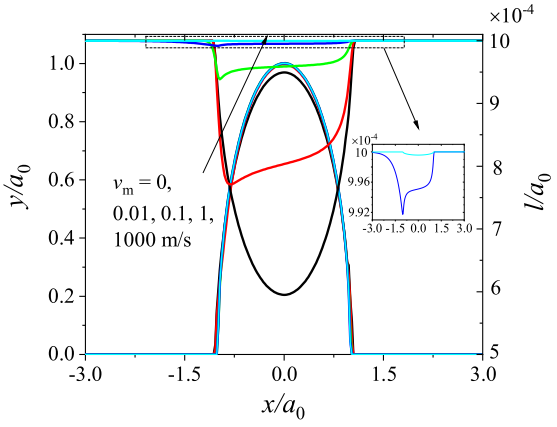

Fig. 17. Pressure and layer thickness distribution along the central line at different rolling velocities predicted by foundation approach of viscoelastic layer modeling. (The ratio of the elastic limits is $E^c_\infty/E^c_0 = 1000$ for the SLS layer; the right side is the rolling entrance.)

results in a relatively constant film thickness in the contact zone. Close to the exit boundary at $x/a_0 = -1$, the local low pressure deforms the viscoelastic layer at a high rate resulting in a rapid decrease in the film thickness as what happened in the inlet region when the layer just goes into the pressurized zone. At location $x/a_0 = -1$, the contact pressure becomes zero as a result of the complementary dry contact boundary condition and since then the viscoelastic layer has fully past the pressurized contact zone and then recovers quickly. The compression and recovery effects lead to the local constriction in the film at the outlet. The position of the minimum film thickness corresponds to the position of zero pressure at $x/a_0 = -1$ for the low speed used in this case.

For a higher rolling velocity (higher Deborah number), there is less time for the layer to deform, which results in a thicker film thickness as well as a reduced minimum film thickness peak at $x/a_0 = -1$. This is also well captured by the model considering piezoviscous effect of the layer, as shown in Fig. 17. At extremely low or high speed conditions, e.g. $v_m = 0$ or 1000 m/s, the viscoelastic layered model gives two elastic solutions due to the nature of the viscoelastic material. In the intermediate speeds corresponding to the transition regime of viscoelastic materials, typical EHL film behaviors could be obtained.

The entire shape of the thin viscoelastic layer after deformation is shown in Fig. 18(a) on a contour plot for the case studied in Fig. 16. Amazingly, a typical horse-shoe shaped film is obtained. It looks so similar to a typical EHL film shape as well as the experimental observation in the PDMS viscoelastic layer experiments, see Fig. 18(b) and (c) respectively. Even though the comparison is not quantitative, the current results obtained with the SLS model of a single relaxation time represent the typical features of the EHL film behavior. One may argue that there is a "boundary layer" around the contact where pressure flow and mass flow conservation dominate, which appears as the inlet pressure rise (sweep), and a decrease in the outlet region preceded by a pressure spike, which is challenging to approximate correctly using viscoelastic layer modeling. However, these cases are not the aim. It is the regime of heavily loaded and heavily starved EHL contacts in which e.g. the contact runs on a grease thickener rich layer augmented with some base oil. In those cases the pressure distribution is very close to the Hertzian with little pressure flow effects. In any case, the above analysis provides a perspective as to when the concept of modeling EHL in the heavily starved regime via viscoelasticity proposed by van Emden et al. [6] might work, e.g. when the piezoviscosity property of the viscoelastic layer is taken into account. The approach also has the potential to be an alternative to model the discontinuous films in mixed lubrication, and/or lubricants with complex rheology. For future work, a nonlinear viscoelasticity layered model needs to be developed for a better description of the EHL behavior and it can be used to model mixed lubrication using discontinuous heterogeneous layers.

6. Conclusion

In this work, the elastic/viscoelastic layered rolling contact problem has been studied using two different modeling approaches, i.e. the foundation (Winkler) reduced model and the full 3D Navier–Cauchy based model using Papkovich–Neuber potentials. The study focused on the behavior of thin layers, the results on pressure distribution, and layer deformation. The differences between the predictions of the two models are shown and discussed for an elastic and viscoelastic layer. A parameter study is presented in which the effects of various (dimensionless) parameters in the models of the SLS viscoelastic layer model and the elastic substrate, e.g. the elasticity ratio of the layer and substrate, the Deborah number, and the elastic limits of the viscoelastic SLS model, on the contact pressure, layer deformation and contact stresses have been studied.

For very thin layers the contact pressure is mostly determined by the substrate material, and closely to Hertzian for an elastic substrate. The layer exhibits constant stresses across the layer, common for thin layers. The main differences are observed in the layer deformation. The foundation model predicts higher layer deformation in view of its local support nature which makes it well suited for soft polymer or grease thickener layers. However, for stiffer layers non-local support bending effects reduce deformation and may even lead to layer thickening. The effects of viscoelasticity are seen in the asymmetry of the deformation and stresses in relation to the contact center. The results presented in this paper provide an overview of layer behavior and are of relevance by themselves for problems in the dry contact regime, with extension to lubricated contacts in the heavily starved regime, or where the contact operates on soft layers like grease thickener layers.

The results also provide a framework of interpretation for the results of van Emden et al. [6] where typical EHL phenomena were observed in a layered contact model with pressure dependent viscosity. The present paper allows a view of these results in the perspective of viscoelastic layered contact behavior. It is shown that to mimic such typical EHL aspects occurring in a layer one needs non-constant (pressure dependent) layer properties, as were indeed assumed by van Emden et al. [6]. The results presented in the present paper also provide an excellent dataset for further research in particular for experimental validation which is the topic of future research.

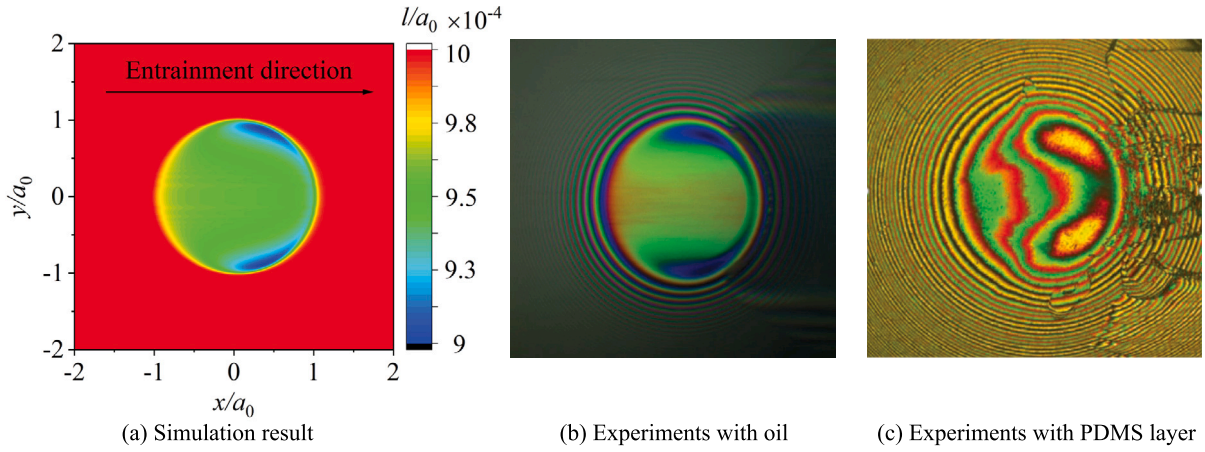

Fig. 18. Qualitative comparison between simulation and experimental results: (a) simulated film shape with the foundation viscoelastic layered model considering piezoviscosity of the layer, (b) measured film shape with oil HVI60 by optical interferometry, (c) measured deformed layer shape with a PDMS layer of initial thickness of 20 μm, no oil.

CRediT authorship contribution statement

Y. Zhao: Conceptualization, Methodology, Software, Draft manuscript preparation, Analysis and interpretation of results. **H.C. Liu**: Conceptualization, Methodology, Analysis and interpretation of results. **G.E. Morales-Espejel**: Conceptualization, Methodology. **C.H. Venner**: Conceptualization, Methodology, Software, Analysis and interpretation of results, Supervision. All the authors have contributed to the writing and editing of the manuscript.

Declaration of competing interest

The authors declare that they have no known competing financial interests or personal relationships that could have appeared to influence the work reported in this paper.

Data availability

Data will be made available on request.

Acknowledgments

The first author wishes to thank Dr. Binbin Zhang of the University of Twente for debugging the program. The first author acknowledges the support of the China Scholarship Council. This research was also supported by SKF Research and Technology Development, Houten, the Netherlands. The authors would like to thank Mr. Bernie van Leeuwen, Director, for his kind permission to publish this article. The authors would like to thank. W. Lette and B. Siemerink for the technical support of the experimental research.

Appendix A. Potential solution verification

The Potential solution is validated with three types of contact problems using reduced versions of the model in this section. The first is the elastic layer-elastic substrate system, the second the viscoelastic half-space (no layer), and the third the viscoelastic layer-elastic substrate system. Subsequently, the calculated layer thickness results obtained with the foundation approach are compared with the PN results.

A.1. Elastic layer-elastic substrate system

The pressure profiles in an elastic layer elastic half-space contact are compared with the results published by O'Sullivan and King [46]. The developed viscoelastic layer model can easily be reduced to the elastic case with a layer modulus of E_0^c by setting $E_\infty^c = E_0^c$ in the creep compliance function of the SLS model, Eq. (2). The same parameters as in [46] have been used: an elastic layer with thickness of $l_0 = a_0$ where a_0 is the Hertzian contact radius calculated with the properties of the elastic substrate. A Poisson ratio of $\nu^c = \nu^s = 0.3$ is assumed, and varying ratios of E_0^c/E^s are considered by using different values of E_0^c at a fixed E^s as input. The pressure distribution along the central line in the x direction is compared in Fig. A.1. The markers indicate the solution in [46] and the solid lines are the results obtained from the developed solver. A good agreement is observed. When the elastic modulus of the substrate is larger than the elastic modulus of the coating, the contact radius reduces and the maximum pressure increases relative to the reference pressure.

A.2. Viscoelastic half-space

Next the developed potential model is reduced to a viscoelastic half-space contact by setting the thickness of the viscoelastic layer to a very large value ($1000a_0$). The results are compared with numerical results of Carbone and Putignano [48] using the FVM methods and of our previous work [36] using the MG integral methods. The operating conditions are $E_\infty^c = 10$ MPa, $E_\infty^c/E_0^c = 10$, $R_0 = 10$ mm, $W_0 = 0.15$ N and $\tau = 0.01$ s. The contact pressure is calculated for a range of dimensionless velocities (Deborah number) $De = \tau/(a_0/v_m)$ with $0 \le De \le 3\times10^4$, where a_0 is the Hertzian contact radius at an extremely low velocity with a modulus of E_0^c [48]. Fig. A.2 shows the pressure distribution along the centerline. The agreement is very good for all numerical models and values of De.

A.3. Viscoelastic layer-elastic substrate system

The developed potential solution is validated by comparing with the simulation results presented by Zhang et al. [28] for a viscoelastic layered rolling contact problem, see Fig. A.3. The parameters are taken identical as in [28]: a (relatively thick) layer thickness of $l_0 = a_0$ where a_0 is the Hertzian contact radius in terms of the properties of the elastic substrate, a normal load of $W_0 = 1.48$ N, a rigid sphere of radius $R_0 = 10$ mm, Poisson ratio of $\nu^c = \nu^s = 0.3$, modulus $E_\infty^c = 10^8$ Pa, $E_\infty^c/E_0^c = 10$ in the SLS model, a single relaxation time $\tau = 0.01$ s and

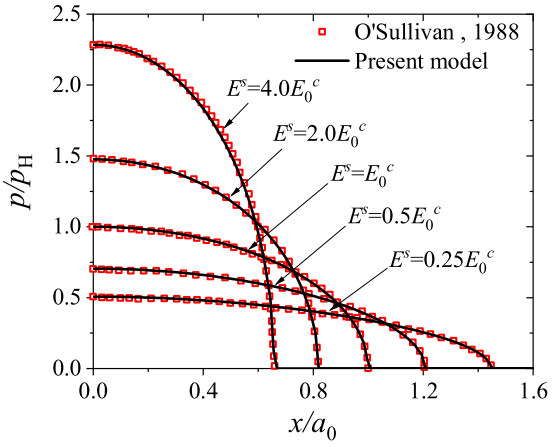

Fig. A.1. Comparison of the normalized pressure profiles with the data in [46] for the contact between a rigid sphere and an elastic layered half-space with layer thickness of a_0. a_0 and p_H are the Hertzian solution calculated with elastic properties of the substrate.

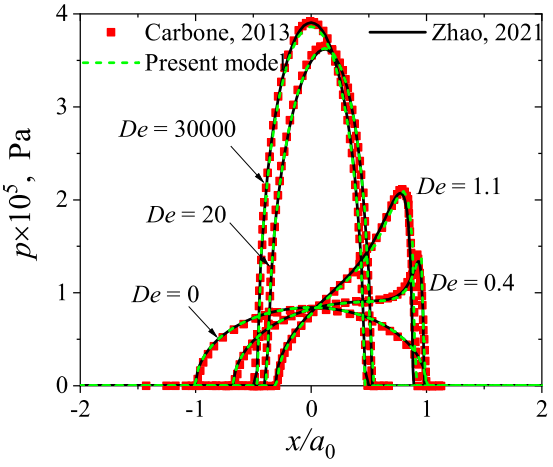

Fig. A.2. Comparison of pressure distribution from the present model (lines) with results of Carbone and Putignano [48] and our previous work [36] for a viscoelastic half-space at a wide range of rolling velocities. (Note the right side is the rolling entrance.)

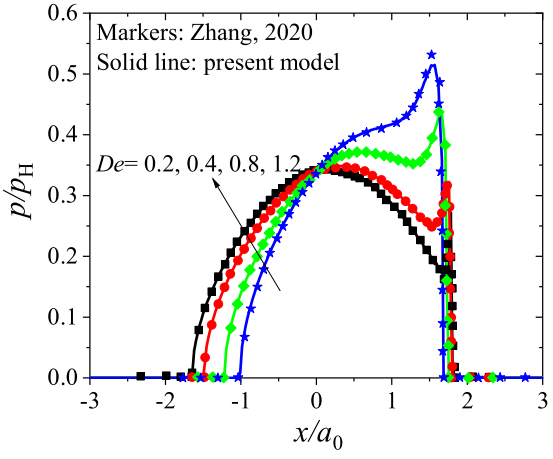

Fig. A.3. Comparison of pressure distribution from the present model (lines) with those from Zhang et al. [28] for viscoelastic layered contacts at different De. (Layer thickness of $l_0 = a_0$; the right side is the rolling entrance.)

the elastic modulus of the substrate $E^s = 2E^c_\infty$. Fig. A.3 shows that a good agreement is achieved for the pressure distribution at different values of De.

Appendix B. Viscoelastic properties

B.1. Fundamentals of viscoelasticity

Viscoelastic materials show significant time-delayed response due to their time-dependent physical–mechanical properties, thus, the current state, e.g. the stress or the strain, of a viscoelastic material is the result of the entire history. Similar to the definition of the compliance and the elastic modulus in the theory of linear elasticity, two time-dependent functions, the creep compliance function $\varphi_c(t)$ and the relaxation modulus function $\psi_r(t)$, are defined to characterize the response of viscoelastic materials [49,50] in viscoelasticity. The creep test with a constant stress as input and the relaxation test with a constant strain as input are usually carried out to determine the creep compliance function $\varphi_c(t)$ and the relaxation modulus function $\psi_r(t)$, respectively.

For constant strain and stress inputs, the stress and the strain response of a specific viscoelastic material can be expressed with $\sigma(t) = \psi_r(t)\epsilon_0$ and $\epsilon(t) = \varphi_c(t)\sigma_0$, respectively. While for a time-varying stress input to linear viscoelastic materials, the strain response can be obtained by applying the Boltzmann superposition principle [49]:

$$\epsilon(t) = \int_{0^-}^{t} \varphi_c(t-q)\frac{d\sigma(q)}{dq}dq \tag{B.1}$$

Similarly, the stress response to a time-varying strain input can be expressed as:

$$\sigma(t) = \int_{0^-}^{t} \psi_r(t-q)\frac{d\epsilon(q)}{dq}dq \tag{B.2}$$

The lower limit 0^- of the integration in Eqs. (B.1) and (B.2) indicates that the discontinuity of applications of the stress and the strain at time $t = 0$ also should be taken into account. For details of the derivation of the compliance and relaxation modulus functions, interested readers can refer to [36,49,50]. Applying the Laplace transform to Eqs. (B.1) and (B.2), one obtains

$$\hat{\varphi}_c(s)\hat{\psi}_r(s) = \frac{1}{s^2} \tag{B.3}$$

where s is the variable in the Laplace transform domain. Using the convolution theorem yields,

$$\int_0^t \varphi_c(q)\psi_r(t-q)dq = t \tag{B.4}$$

Note that the relationship of mutual reciprocal in elasticity between the compliance and the elastic modulus is not valid in the time domain for viscoelasticity; instead, it is only valid in the transform domain [49].

Taking Fourier transform of Eq. (B.1), one obtains

$$\hat{\epsilon}(\omega) = i\omega\hat{\varphi}_c(\omega)\hat{\sigma}(\omega) \tag{B.5}$$

where ω is the time-related variable in the Fourier frequency domain. According to the correspondence principle, the relation of the stress and strain in the frequency domain is $\hat{\epsilon}(\omega) = \hat{\sigma}(\omega)/\hat{\psi}_r(\omega)$, which is equivalent to the corresponding elastic one. Hence, the relation of relaxation modulus function $\psi(t)$ and the creep compliance function $\varphi(t)$ of viscoelastic materials in frequency domain is

$$\hat{\psi}_r(\omega) = [i\omega\hat{\varphi}_c(\omega)]^{-1} \tag{B.6}$$

B.2. Frequency response of the SLS model

The frequency response of the material model is obtained by applying the Fourier transform to the differential constitutive equation, Eq. (1):

$$\frac{1}{2\pi}\int_{t=-\infty}^{+\infty}\left[\sigma+\beta\frac{\partial\sigma}{\partial t}\right]e^{i\omega t}\mathrm{d}t = \frac{1}{2\pi}\int_{t=-\infty}^{+\infty}\left[E_0\left(\epsilon+\tau\frac{\partial\epsilon}{\partial t}\right)\right]e^{i\omega t}\mathrm{d}t \tag{B.7}$$

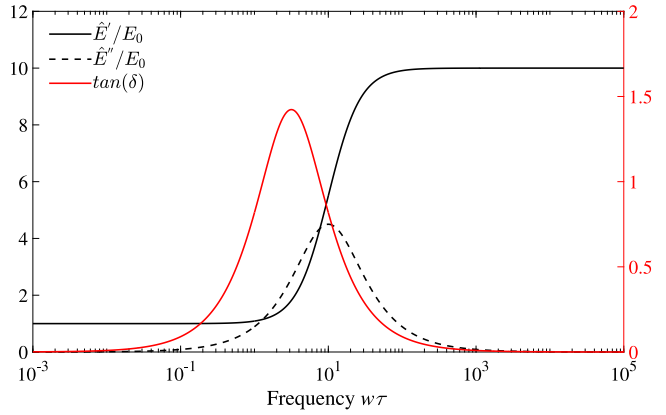

Fig. B.1. Evolution of $\hat{E}'(\omega)/E_0$, $\hat{E}''(\omega)/E_0$ and $tan(\delta)$ for an SLS model with $\tau/\beta = 10$ ($R_e = 9$).

Introducing the following functions in both frequency and time space:

$$\sigma(t) = \int_{\omega=-\infty}^{+\infty} \hat{\sigma}(\omega) e^{-i\omega t} \mathrm{d}\omega, \qquad \hat{\sigma}(\omega) = \frac{1}{2\pi} \int_{t=-\infty}^{+\infty} \sigma(t) e^{i\omega t} \mathrm{d}t$$
$$\epsilon(t) = \int_{\omega=-\infty}^{+\infty} \hat{\epsilon}(\omega) e^{-i\omega t} \mathrm{d}\omega, \qquad \hat{\epsilon}(\omega) = \frac{1}{2\pi} \int_{t=-\infty}^{+\infty} \epsilon(t) e^{i\omega t} \mathrm{d}t \tag{B.8}$$

the material response in frequency is then:

$$\hat{\sigma}(\omega) = E_0 \frac{1 - i\omega\tau}{1 - i\omega\beta} \hat{\epsilon}(\omega) \tag{B.9}$$

Using this relation, the complex modulus is given as:

$$\hat{E}(\omega) = E_0 \frac{1 - i\omega\tau}{1 - i\omega\beta} \tag{B.10}$$

which can be decomposed in real and imaginary parts

$$\hat{E}(\omega) = \hat{E}'(\omega) + i\hat{E}''(\omega) \tag{B.11}$$

Using this definition, the following expressions are obtained:

$$\begin{aligned} \hat{E}'(\omega) &= E_0 \frac{1 + \omega^2\tau\beta}{1 + \omega^2\beta^2} \\ \hat{E}''(\omega) &= E_0 \frac{\omega(\tau - \beta)}{1 + \omega^2\beta^2} \\ tan(\delta) &= \frac{\hat{E}''(\omega)}{\hat{E}'(\omega)} = \frac{\omega(\tau - \beta)}{1 + \omega^2\tau\beta} \end{aligned} \tag{B.12}$$

The evolution of $\hat{E}'(\omega)$, $\hat{E}''(\omega)$ and $tan(\delta)$ as a function of $\omega\tau$ for $\tau/\beta = 10$ ($R_e = 9$) is given in Fig. B.1. It shows that the material exhibits changes in behavior with frequency. At a low frequency, the dashpot does not play any role and the material behaves as a pure elastic material with a rigidity equals to E_0, $\hat{E}'(\omega = 0)/E_0 = 1$. At a high frequency, the dashpot becomes exceedingly rigid and the material response is governed by the modulus E_∞, $\hat{E}'(\omega = \infty)/E_0 = 1 + R_e = 10$. In these two extreme conditions, the viscoelastic dissipation is related to the imaginary part $\hat{E}''(\omega)$, which become negligible and correspondingly the loss angel is close to 0. While, the loss angel $tan(\delta)$ is very large in the intermediate frequency range, and this region determines the energy dissipation during rolling or sliding contacts, as reported in [48],

In viscoelasticity, the real part $\hat{E}'(\omega)$ and the imaginary part $\hat{E}''(\omega)$ in Eq. (B.11) are defined as storage modulus and loss modulus, separately. And their ratio $tan(\delta)$ is named as loss angel, which are usually used to characterize the dynamic response of the viscoelastic materials [49]. The dynamic response indicates the response in a dynamic test, in which the stress (or strain) resulting from a sinusoidal strain (or stress) is measured [49,51].

Appendix C. Frequency response of elastic layered half-space

C.1. Displacement and stress components

The elastic displacement and stress components in the frequency domain can be derived from Eq. (22) as following:

The displacement components are,

$$\begin{aligned} \tilde{\bar{u}}_1^k =& \frac{1}{2\mu^k} \Big\{ im(A^k e^{-\alpha z^k} + \bar{A}^k e^{\alpha z^k}) - 4(1-\nu^k)(B^k e^{-\alpha z^k} + \bar{B}^k e^{\alpha z^k}) + m^2\alpha^{-1} z^k \\ & (B^k e^{-\alpha z^k} - \bar{B}^k e^{\alpha z^k}) + imz^k (C^k e^{-\alpha z^k} + \bar{C}^k e^{\alpha z^k}) \\ & - m(B_{,m}^k e^{-\alpha z^k} + \bar{B}_{,m}^k e^{\alpha z^k}) \Big\} \end{aligned} \tag{C.1}$$

$$\begin{aligned} \tilde{\bar{u}}_2^k =& \frac{1}{2\mu^k} \Big\{ in(A^k e^{-\alpha z^k} + \bar{A}^k e^{\alpha z^k}) + mn\alpha^{-1} z^k (B^k e^{-\alpha z^k} - \bar{B}^k e^{\alpha z^k}) \\ & + inz^k (C^k e^{-\alpha z^k} + \bar{C}^k e^{\alpha z^k}) - n(B_{,m}^k e^{-\alpha z^k} + \bar{B}_{,m}^k e^{\alpha z^k}) \Big\} \end{aligned} \tag{C.2}$$

$$\begin{aligned} \tilde{\bar{u}}_3^k =& \frac{1}{2\mu^k} \Big\{ -\alpha(A^k e^{-\alpha z^k} - \bar{A}^k e^{\alpha z^k}) + imz^k (B^k e^{-\alpha z^k} + \bar{B}^k e^{\alpha z^k}) \\ & - im\alpha^{-1} (B^k e^{-\alpha z^k} - \bar{B}^k e^{\alpha z^k}) \\ & - (3 - 4\nu^k)(C^k e^{-\alpha z^k} + \bar{C}^k e^{\alpha z^k}) - \alpha z^k (C^k e^{-\alpha z^k} - \bar{C}^k e^{\alpha z^k}) \\ & - i\alpha (B_{,m}^k e^{-\alpha z^k} - \bar{B}_{,m}^k e^{\alpha z^k}) \Big\} \end{aligned} \tag{C.3}$$

The stress components are,

$$\begin{aligned} \tilde{\bar{\sigma}}_{11}^k =& -m^2(A^k e^{-\alpha z^k} + \bar{A}^k e^{\alpha z^k}) + 2im(\upsilon^k - 2)(B^k e^{-\alpha z^k} + \bar{B}^k e^{\alpha z^k}) \\ & + im^3\alpha^{-1} z^k (B^k e^{-\alpha z^k} - \bar{B}^k e^{\alpha z^k}) - m^2 z^k (C^k e^{-\alpha z^k} + \bar{C}^k e^{\alpha z^k}) \\ & + 2\alpha\upsilon^k (C^k e^{-\alpha z^k} - \bar{C}^k e^{\alpha z^k}) - im^2 (B_{,m}^k e^{-\alpha z^k} + \bar{B}_{,m}^k e^{\alpha z^k}) \end{aligned} \tag{C.4}$$

$$\begin{aligned} \tilde{\bar{\sigma}}_{22}^k =& -n^2(A^k e^{-\alpha z^k} + \bar{A}^k e^{\alpha z^k}) - 2im\upsilon^k (B^k e^{-\alpha z^k} + \bar{B}^k e^{\alpha z^k}) \\ & + imn^2\alpha^{-1} z^k (B^k e^{-\alpha z^k} - \bar{B}^k e^{\alpha z^k}) - n^2 z^k (C^k e^{-\alpha z^k} + \bar{C}^k e^{\alpha z^k}) \\ & + 2\alpha\upsilon^k (C^k e^{-\alpha z^k} - \bar{C}^k e^{\alpha z^k}) - in^2 (B_{,m}^k e^{-\alpha z^k} + \bar{B}_{,m}^k e^{\alpha z^k}) \end{aligned} \tag{C.5}$$

$$\begin{aligned} \tilde{\bar{\sigma}}_{33}^k =& \alpha^2(A^k e^{-\alpha z^k} + \bar{A}^k e^{\alpha z^k}) + 2im(1 - \upsilon^k)(B^k e^{-\alpha z^k} + \bar{B}^k e^{\alpha z^k}) \\ & - im\alpha z^k (B^k e^{-\alpha z^k} - \bar{B}^k e^{\alpha z^k}) + \alpha^2 z^k (C^k e^{-\alpha z^k} + \bar{C}^k e^{\alpha z^k}) \\ & + 2\alpha(1 - \upsilon^k)(C^k e^{-\alpha z^k} - \bar{C}^k e^{\alpha z^k}) + i\alpha^2 (B_{,m}^k e^{-\alpha z^k} + \bar{B}_{,m}^k e^{\alpha z^k}) \end{aligned} \tag{C.6}$$

$$\begin{aligned} \tilde{\bar{\sigma}}_{12}^k =& -mn(A^k e^{-\alpha z^k} + \bar{A}^k e^{\alpha z^k}) - 2in(1 - \upsilon^k)(B^k e^{-\alpha z^k} + \bar{B}^k e^{\alpha z^k}) \\ & + im^2 n\alpha^{-1} z^k (B^k e^{-\alpha z^k} - \bar{B}^k e^{\alpha z^k}) - mnz^k (C^k e^{-\alpha z^k} + \bar{C}^k e^{\alpha z^k}) \\ & - imn(B_{,m}^k e^{-\alpha z^k} + \bar{B}_{,m}^k e^{\alpha z^k}) \end{aligned} \tag{C.7}$$

$$\begin{aligned} \tilde{\bar{\sigma}}_{31}^k =& -im\alpha(A^k e^{-\alpha z^k} + \bar{A}^k e^{\alpha z^k}) - m^2 z^k (B^k e^{-\alpha z^k} + \bar{B}^k e^{\alpha z^k}) \\ & + \left[2\alpha(1 - \upsilon^k) + m^2\alpha^{-1}\right](B^k e^{-\alpha z^k} - \bar{B}^k e^{\alpha z^k}) \\ & - im(1 - 2\upsilon^k)(C^k e^{-\alpha z^k} + \bar{C}^k e^{\alpha z^k}) - im\alpha z^k (C^k e^{-\alpha z^k} - \bar{C}^k e^{\alpha z^k}) \\ & + m\alpha(B_{,m}^k e^{-\alpha z^k} - \bar{B}_{,m}^k e^{\alpha z^k}) \end{aligned} \tag{C.8}$$

$$\begin{aligned} \tilde{\bar{\sigma}}_{32}^k =& -in\alpha(A^k e^{-\alpha z^k} - \bar{A}^k e^{\alpha z^k}) - mnz^k (B^k e^{-\alpha z^k} + \bar{B}^k e^{\alpha z^k}) \\ & + mn\alpha^{-1}(B^k e^{-\alpha z^k} - \bar{B}^k e^{\alpha z^k}) - in(1 - 2\upsilon^k)(C^k e^{-\alpha z^k} + \bar{C}^k e^{\alpha z^k}) \\ & - in\alpha z^k (C^k e^{-\alpha z^k} - \bar{C}^k e^{\alpha z^k}) + n\alpha(B_{,m}^k e^{-\alpha z^k} - \bar{B}_{,m}^k e^{\alpha z^k}) \end{aligned} \tag{C.9}$$

where $\alpha = \sqrt{m^2 + n^2}$ with m and n being the Fourier transform variables corresponding to x and y, respectively. The letter i in the above equations is the imaginary unit.

C.2. Coefficients in Papkovich–Neuber potentials

The Fourier transform of Papkovich–Neuber potentials, Eq. (21), shows that 12 unknown coefficients A^k, B^k, C^k, $\bar{A}^k$, $\bar{B}^k$ and $\bar{C}^k$ with $k = c$ or $k = s$ need to be determined in order to solve the problem. Following the description in [38,39], the analytical expressions of the coefficients are given in this section. The condition that the displacements and stresses should vanish at infinite in z direction in the

substrate indicates that $\bar{A}^s = \bar{B}^s = \bar{C}^s = 0$. And the rest nine coefficients in Eq. (21) can be obtained by solving the boundary conditions given by Eqs. (19) and (20).

With the following definition,

$$\begin{aligned}\alpha &= \sqrt{m^2+n^2}\\ \theta &= e^{-2\alpha l_0}\\ \mu_{cs} &= \frac{\mu^c}{\mu^s}\end{aligned} \tag{C.10}$$

the B components and its related derivatives are

$$\bar{B}^c = -\frac{\tilde{\bar{q}}_x\theta(t_4\mu_{cs}-t_1)}{2\alpha(1-\mu^c)\left[(t_4\mu_{cs}+t_1)-\theta(t_4\mu_{cs}-t_1)\right]} \tag{C.11}$$

$$\bar{B}^c_{,m} = \frac{\tilde{\bar{q}}_x m\theta(t_4\mu_{cs}-t_1)\left[(1+2\alpha l_0)(t_4\mu_{cs}+t_1)-\theta(t_4\mu_{cs}-t_1)\right]}{2\alpha^3(1-\mu^c)\left[(t_4\mu_{cs}+t_1)-\theta(t_4\mu_{cs}-t_1)\right]^2} \tag{C.12}$$

$$B^c = \bar{B}^c - \frac{\tilde{\bar{q}}_x}{2\alpha(1-\mu^c)} \tag{C.13}$$

$$B^c_{,m} = \bar{B}^c_{,m} + \frac{\tilde{\bar{q}}_x m}{2\alpha^3(1-\mu^c)} \tag{C.14}$$

$$B^s = \frac{t_4(1-\mu^c)(\theta-1)}{1-\mu^s}\bar{B}^c e^{\alpha l_0} - \frac{\tilde{\bar{q}}_x t_4 e^{-\alpha l_0}}{2\alpha(1-\mu^s)} \tag{C.15}$$

$$\begin{aligned}B^s_{,m} = &-\frac{t_4(1-\mu^c)}{(1-\mu^s)}\frac{ml_0(1+\theta)}{\alpha}\bar{B}^c e^{\alpha l_0} + \frac{t_4(1-\mu^c)(\theta-1)}{(1-\mu^s)}\bar{B}^c_{,m}e^{\alpha l_0}\\ &+\frac{\tilde{\bar{q}}_x(1+\alpha l_0)t_4 m e^{-\alpha l_0}}{2\alpha^3(1-\mu^s)}\end{aligned} \tag{C.16}$$

where $\tilde{\bar{q}}_x$ is the Fourier transforms of shear traction with respect to x and y. Note that all B items will be zero for frictionless rolling contact, as reported in [28].

The A and C components are

$$A^c = \frac{S_2 + \alpha\bar{A}^c - (1-2\nu^c)C^c - (1-2\nu^c)\bar{C}^c}{\alpha} \tag{C.17}$$

$$\bar{A}^c = \frac{1}{2\alpha}\left[(S_1-S_2) - C^c - (4\mu^c-3)\bar{C}^c\right] \tag{C.18}$$

$$C^c = \frac{S_c - k_{16}\bar{C}^c}{k_{15}} \tag{C.19}$$

$$\bar{C}^c = \frac{k_{15}S_d - k_{17}S_c}{k_{15}k_{18} - k_{16}k_{17}} \tag{C.20}$$

$$A^s = \frac{t_1}{\mu_{cs}}(e^{-\alpha l_0}A^c + e^{\alpha l_0}\bar{A}^c + l_0 e^{-\alpha l_0}C^c + l_0 e^{\alpha l_0}\bar{C}^c - \frac{\mu^c S_3}{t_1}) \tag{C.21}$$

$$\begin{aligned}C^s = \frac{1}{2(1-\mu^s)}\{&t_6\alpha e^{-\alpha l_0}A^c + t_6\alpha e^{\alpha l_0}\bar{A}^c + t_6[2(1-\mu^c)+\alpha l_0]e^{-\alpha l_0}C^c\\ &-t_6[2(1-\mu^c)-\alpha l_0]e^{\alpha l_0}\bar{C}^c - \alpha A^s - S_6\}\end{aligned} \tag{C.22}$$

where

$$\begin{aligned}k_{15}S_d - k_{17}S_c = &\left(k_{10}-\frac{k_9}{2\alpha}\right)\left(S_b - \frac{k_5}{\alpha}S_2 - \frac{k_{12}}{2\alpha}(S_1-S_2)\right)\\ &-\left(k_{13}-\frac{k_{12}}{2\alpha}\right)\left(S_a - \frac{k_1}{\alpha}S_2 - \frac{k_9}{2\alpha}(S_1-S_2)\right)\end{aligned} \tag{C.23}$$

The S components are

$$S_1 = \frac{i}{\alpha}\left[i\tilde{\bar{p}} - 2m(1-\mu^c)(B^c+\bar{B}^c) - \alpha^2(B^c_{,m}+\bar{B}^c_{,m})\right] \tag{C.24}$$

where $\tilde{\bar{p}}$ is the Fourier transforms of pressure.

$$S_2 = \frac{i}{\alpha}\left[-m(B^c-\bar{B}^c) - \alpha^2(B^c_{,m}+\bar{B}^c_{,m})\right] \tag{C.25}$$

$$S_3 = \frac{i}{\alpha}\left[\frac{t_1 ml_0}{\mu^c}(B^c e^{-\alpha l_0} - \bar{B}^c e^{\alpha l_0}) - \frac{t_1\alpha}{\mu^c}(B^c_{,m}e^{-\alpha l_0} + \bar{B}^c_{,m}e^{\alpha l_0}) + \frac{\alpha}{\mu^s}B^s_{,m}\right] \tag{C.26}$$

$$\begin{aligned}S_4 = \frac{i}{\alpha}\Big[&-\frac{t_3 m\alpha l_0}{\mu^c}(B^c e^{-\alpha l_0} + \bar{B}^c e^{\alpha l_0}) + \frac{t_3 m}{\mu^c}(B^c e^{-\alpha l_0} - \bar{B}^c e^{\alpha l_0})\\ &+\frac{t_3\alpha^2}{\mu^c}(B^c_{,m}e^{-\alpha l_0} - \bar{B}^c_{,m}e^{\alpha l_0}) - \frac{m}{\mu^s}B^s - \frac{\alpha^2}{\mu^s}B^s_{,m}\Big]\end{aligned} \tag{C.27}$$

$$\begin{aligned}S_5 = \frac{i}{\alpha}\Big[&-(1-\alpha l_0)t_4 m B^c e^{-\alpha l_0} + (1+\alpha l_0)t_4 m\bar{B}^c e^{\alpha l_0}\\ &-t_4\alpha^2(B^c_{,m}e^{-\alpha l_0} - \bar{B}^c_{,m}e^{\alpha l_0}) + mB^s + \alpha^2 B^s_{,m}\Big]\end{aligned} \tag{C.28}$$

$$\begin{aligned}S_6 = \frac{i}{\alpha}\Big[&-2t_6 m(1-\mu^c)(B^c e^{-\alpha l_0} + \bar{B}^c e^{\alpha l_0}) + t_6 m\alpha l_0(B^c e^{-\alpha l_0} - \bar{B}^c e^{\alpha l_0})\\ &-t_6\alpha^2(B^c_{,m}e^{-\alpha l_0} + \bar{B}^c_{,m}e^{\alpha l_0}) + 2m(1-\mu^s)B^s + \alpha^2 B^s_{,m}\Big]\end{aligned} \tag{C.29}$$

$$S_a = \frac{\mu^c}{2(1-\mu^s)t_3}S_4 e^{-\alpha l_0} - \frac{(1-2\mu^s)\mu_{cs}}{2(1-\mu^s)t_3}S_5 e^{-\alpha l_0} + \frac{\mu_{cs}}{t_3}S_6 e^{-\alpha l_0} \tag{C.30}$$

$$S_b = \frac{\alpha\mu^c}{t_1}S_3 e^{-\alpha l_0} - \frac{(1-2\mu^s)\mu_{cs}}{t_1}S_5 e^{-\alpha l_0} + \frac{2(1-\mu^s)\mu_{cs}}{t_1}S_6 e^{-\alpha l_0} \tag{C.31}$$

$$S_c = S_a - \frac{k_1}{\alpha}S_2 - \frac{k_9}{2\alpha}(S_1-S_2) \tag{C.32}$$

$$S_d = S_b - \frac{k_5}{\alpha}S_2 - \frac{k_{12}}{2\alpha}(S_1-S_2) \tag{C.33}$$

The intermediate variables are

$$k_1 = \left(\frac{t_6\mu_{cs}}{t_3}-1\right)\alpha\theta - \frac{1-2\mu^s}{2-2\mu^s}\left(\frac{t_4\mu_{cs}}{t_3}-1\right)\alpha\theta \tag{C.34}$$

$$k_2 = \left(\frac{t_6\mu_{cs}}{t_3}+1\right)\alpha + \frac{1-2\mu^s}{2-2\mu^s}\left(\frac{t_4\mu_{cs}}{t_3}-1\right)\alpha \tag{C.35}$$

$$\begin{aligned}k_3 = &[2(1-\mu^c)+\alpha l_0]\frac{t_6\mu_{cs}\theta}{t_3} - (3-4\mu^c+\alpha l_0)\theta\\ &-\frac{(1-2\mu^s)\theta}{2-2\mu^s}\left((1-2\mu^c+\alpha l_0)\frac{t_4\mu_{cs}}{t_3} - (3-4\mu^c+\alpha l_0)\right)\end{aligned} \tag{C.36}$$

$$\begin{aligned}k_4 = &-[2(1-\mu^c)-\alpha l_0]\frac{t_6\mu_{cs}}{t_3} - (3-4\mu^c-\alpha l_0)\\ &-\frac{1-2\mu^s}{2-2\mu^s}\left((1-2\mu^c+\alpha l_0)\frac{t_4\mu_{cs}}{t_3} - (3-4\mu^c-\alpha l_0)\right)\end{aligned} \tag{C.37}$$

$$k_5 = \alpha\theta + \frac{\mu_{cs}\alpha\theta}{t_1}[(1-2\mu^s)t_6 - 2(1-\mu^s)t_4] \tag{C.38}$$

$$k_6 = \alpha + \frac{\mu_{cs}\alpha}{t_1}[(1-2\mu^s)t_6 + 2(1-\mu^s)t_4] \tag{C.39}$$

$$k_7 = \alpha l_0\theta + \frac{(1-2\mu^s)\mu_{cs}\theta}{t_1}\left\{[2(1-\mu^c)+\alpha l_0]t_6 - \frac{2(1-\mu^s)(1-2\mu^c+\alpha l_0)t_4}{1-2\mu^s}\right\} \tag{C.40}$$

$$k_8 = \alpha l_0 - \frac{(1-2\mu^s)\mu_{cs}}{t_1}\left\{[2(1-\mu^c)-\alpha l_0]t_6 + \frac{2(1-\mu^s)(1-2\mu^c-\alpha l_0)t_4}{1-2\mu^s}\right\} \tag{C.41}$$

$$k_9 = k_1 + k_2 \tag{C.42}$$

$$k_{10} = k_3 - \frac{k_1}{\alpha}(1-2\mu^c) \tag{C.43}$$

$$k_{11} = k_4 - \frac{k_1}{\alpha}(1-2\mu^c) \tag{C.44}$$

$$k_{12} = k_5 + k_6 \tag{C.45}$$

$$k_{13} = k_7 - \frac{k_5}{\alpha}(1-2\mu^c) \tag{C.46}$$

$$k_{14} = k_8 - \frac{k_5}{\alpha}(1-2\mu^c) \tag{C.47}$$

$$k_{15} = k_{10} - \frac{k_9}{2\alpha} \tag{C.48}$$

$$k_{16} = k_{11} - \frac{k_9}{2\alpha}(4\mu^c - 3) \tag{C.49}$$

$$k_{17} = k_{13} - \frac{k_{12}}{2\alpha} \tag{C.50}$$

$$k_{18} = k_{14} - \frac{k_{12}}{2\alpha}(4\mu^c - 3) \tag{C.51}$$

Appendix D. Green's function analysis

The correspondence principle proposed by Alfrey [43] implies that the viscoelastic solution to a problem can be derived from an appropriate elastic solution. Taking the point contact problem on a half-space as an example, the elastic deformation equation can be calculated by the Boussinesq equation,

$$u(x,y) = \iint G_E(x-x', y-y')p(x',y')\mathrm{d}x'\mathrm{d}y' \tag{D.1}$$

where $G_E(x,y) = \frac{1-\nu^2}{\pi E}\frac{1}{\sqrt{x^2+y^2}}$ is the elastic Green's function. As reported in [48,52] and also our previous work [36], the deformation equation for a viscoelastic half-space can be derived from Eq. (D.1), which is

$$u(x,y,t) = \int_{-\infty}^{t}\iint G_{VE}(x-x', y-y', t-q)\frac{\partial p(x',y',q)}{\partial q}\mathrm{d}x'\mathrm{d}y'dq \tag{D.2}$$

where $G_{VE}(x,y,t) = \frac{(1-\nu^2)\varphi_c(t)}{\pi}\frac{1}{\sqrt{x^2+y^2}}$ is the viscoelastic Green's function. The above two equations, Eqs. (D.1) and (D.2), show that the time-dependent viscoelastic Green's function G_{VE} can be easily derived from elastic Green's function by replacing the compliance, $1/E$, with compliance function, $\varphi_c(t)$, in G_E. Furthermore, the time-dependent viscoelastic deformation equation, Eq. (D.2), can be used to describe the steady-state response under rolling/sliding conditions with the following relations

$$u(x,y,t) = u(x + v_m t, y) \tag{D.3}$$

$$p(x,y,t) = p(x + v_m t, y) \tag{D.4}$$

Applying double Fourier transform to Eq. (D.1), which gives

$$\tilde{\tilde{u}}(m,n) = \tilde{\tilde{G}}_E(m,n)\tilde{\tilde{p}}(m,n) \tag{D.5}$$

where $\tilde{\tilde{G}}_E(m,n) = \frac{1-\nu^2}{\pi E}\frac{1}{\sqrt{m^2+n^2}}$ is the Fourier transformed elastic Green's function, and m and n being the transformed variables with respect to x and y, respectively. Applying triple Fourier transforms to Eqs. (D.2)~(D.4) with respect to t, x and y, respectively, leads to the following

$$\tilde{\tilde{\tilde{u}}}(m,n,w) = \tilde{\tilde{\tilde{G}}}^*_{VE}(m,n,w)\tilde{\tilde{\tilde{p}}}(m,n,w) \tag{D.6}$$

$$\tilde{\tilde{\tilde{u}}}(m,n,w) = 2\pi\delta(w - mv_m)\tilde{\tilde{u}}(m,n) \tag{D.7}$$

$$\tilde{\tilde{\tilde{p}}}(m,n,w) = 2\pi\delta(w - mv_m)\tilde{\tilde{p}}(m,n) \tag{D.8}$$

where $\tilde{\tilde{\tilde{G}}}^*_{VE} = iw\tilde{\tilde{\tilde{G}}}_{VE}$ in Eq. (D.6) is Fourier transformed viscoelastic Green's function, $\delta(w - mv_m)$ in Eqs. (D.7) and (D.8) being the Dirac delta function and w being the time-related variable in transformed domain.

Substituting Eqs. (D.7) and (D.8) into Eq. (D.6), the following equation is obtained

$$\tilde{\tilde{u}}(m,n) = \tilde{\tilde{\tilde{G}}}^*_{VE}(m,n,mv_m)\tilde{\tilde{p}}(m,n) \tag{D.9}$$

This equation shows that the time-dependent viscoelastic deformation can be transferred to a speed-dependent problem with the relation $w = mv_m$. And the viscoelastic problem can be readily solved by replacing $G_E(m,n)$ with $\tilde{\tilde{\tilde{G}}}^*_{VE}(m,n,mv_m)$ in the corresponding elastic solution. In addition, the steady-state viscoelastic Green's function in the transformed domain $\tilde{\tilde{\tilde{G}}}^*_{VE}(m,n,mv_m)$ can be directly obtained by replacing the elastic modulus E with relaxation function $\psi_r(w = mv_m)$ in elastic Green's function $\tilde{\tilde{G}}_E(m,n)$.

References

[1] Cann PM. Grease lubrication of rolling element bearings—role of the grease thickener. Lubr Sci 2007;19(3):183–96.
[2] Cyriac F, Lugt PM, Bosman R, Padberg CJ, Venner CH. Effect of thickener particle geometry and concentration on the grease EHL film thickness at medium speeds. Tribol Lett 2016;61(2):1–13.
[3] Dorgham A, Wang C, Morina A, Neville A. Local occupancy of viscoelastic interfaces: a new rheological respctive on antiwear tribofilms. In: 44th leeds-lyon symposium on tribology. 2017.
[4] Zhang B, Boffy H, Venner CH. Multigrid solution of 2D and 3D stress fields in contact mechanics of anisotropic inhomogeneous materials. Tribol Int 2020;149:105636.
[5] Argatov I, Mishuris G. Contact mechanics of articular cartilage layers. Springer; 2015.
[6] van Emden E, Venner CH, Morales-Espejel GE. Investigation into the viscoelastic behaviour of a thin lubricant layer in an EHL contact. Tribol Int 2017;111:197–210.
[7] Alsaad M, Bair S, Sanborn DM, Winer WO. Glass transitions in lubricants: Its relation to elastohydrodynamic lubrication (EHD). J Lubr Technol 1978;100(3):404–16.
[8] Bair S. The viscosity at the glass transition of a liquid lubricant. Friction 2018;7(1):86–91,.
[9] Reiter G, Demirel AL, Granick S. From static to kinetic friction in confined liquid films. Science 1994;263(5154):1741–4.
[10] Hu YZ, Granick S. Microscopic study of thin film lubrication and its contributions to macroscopic tribology. Tribol Lett 1998;5(1):81–8.
[11] Otsu T, Imado K. Study on changes in the rheologic properties of EHL film using fluorescence measurements. Tribol Lett 2018;66(1):1–10.
[12] Ohno N. High-pressure behavior of toroidal CVT fluid for automobile. Tribol Int 2007;40(2):233–8.
[13] Bair S, Khonsari M, Winer WO. High-pressure rheology of lubricants and limitations of the Reynolds equation. Tribol Int 1998;31(10):573–86.
[14] Venner CH, Lubrecht AA. Multi-level methods in lubrication, vol. 37. Elsevier; 2000.
[15] Alblas JB, Kuipers M. The contact problem of a rigid cylinder rolling on a thin viscoelastic layer. Internat J Engrg Sci 1970;8(5):363–80.
[16] Naghieh GR, Jin ZM, Rahnejat H. Contact characteristics of viscoelastic bonded layers. Appl Math Model 1998;22(8):569–81,.
[17] Putignano C, Carbone G, Dini D. Mechanics of rough contacts in elastic and viscoelastic thin layers. Int J Solids Struct 2015;69–70:507–17.
[18] Essink MH, Pandey A, Karpitschka S, Venner CH, Snoeijer JH. Regimes of soft lubrication. J Fluid Mech 2021;915.
[19] Altenbach H, Goldstein RV, Murashkin E. Mechanics for materials and technologies. Advanced Structured Materials, vol. 46, Springer; 2017.
[20] Menga N, Afferrante L, Carbone G. Effect of thickness and boundary conditions on the behavior of viscoelastic layers in sliding contact with wavy profiles. J Mech Phys Solids 2016;95:517–29.
[21] Stepanov FI, Torskaya EV. Modeling of sliding of a smooth indenter over a viscoelastic layer coupled with a rigid base. Mech Solids 2018;53(1):60–7,.
[22] Batra SK, Ling FF. On deformation friction and interface shear stress in viscoelastic-elastic layered system under a moving load. ASLE Trans 1967;10(3):294–301.
[23] Kalker JJ. Viscoelastic multilayered cylinders rolling with dry friction. J Appl Mech 1991;58(3):666–79.
[24] Braat GFM, Kalker JJ. Theoretical and experimental analysis of the rolling contact between two cylinders coated with multilayered, viscoelastic rubber. WIT Trans. Eng. Sci. 1970;1:8.
[25] Goryacheva I, Sadeghi F. Contact characteristics of a rolling sliding cylinder and a viscoelastic layer bonded to an elastic substrate. Wear 1995;184(2):125–32.
[26] Goryacheva IG, Goryachev AP, Sadegi F. Contact of elastic bodies with thin visco-elastic coatings under conditions of rolling or sliding friction. J Appl Math Mech 1995;59(4):607–14.
[27] Goryacheva I, Miftakhova A. Modelling of the viscoelastic layer effect in rolling contact. Wear 2019;430:256–62.
[28] Zhang X, Wang QJ, He T. Transient and steady-state viscoelastic contact responses of layer-substrate systems with interfacial imperfections. J Mech Phys Solids 2020;145.
[29] He T, Wang QJ, Zhang X, Liu Y, Li Z, Kim HJ, et al. Visco-elastohydrodynamic lubrication of layered materials with imperfect layer-substrate interfaces. Int J Mech Sci 2021;189.
[30] Wallace ER, Chaise T, Nelias D. Three-dimensional rolling/sliding contact on a viscoelastic layered half-space. J Mech Phys Solids 2020;143.
[31] Wallace ER, Chaise T, Nelias D. Rolling contact on a viscoelastic multi-layered half-space. Int J Solids Struct 2022;239–240.
[32] Wallace ER, Chaise T, Nelias D. Rolling contact on a viscoelastic multi-layered half-space. Int J Solids Struct 2022;239:111388.
[33] Dillard DA, Mukherjee B, Karnal P, Batra RC, Frechette J. A review of Winkler's foundation and its profound influence on adhesion and soft matter applications. Soft Matter 2018;14:3669.

[34] Wijnant YH, Venner CH, Larsson R, Eriksson P. Effects of structural vibrations on the film thickness in an ehl circular contact. J Tribol 1999;121(2):259–64.
[35] Zhao Y, Liu HC, Morales-Espejel GE, Venner CH. Effects of solid viscoelasticity on elastohydrodynamic lubrication of point contacts. Tribol Int 2022;171:107562.
[36] Zhao Y, Morales-Espejel GE, Venner CH. Aspects of modeling and numerical simulation of dry point contacts between viscoelastic solids. Tribol Int 2022;165:107245.
[37] Xi Y, Björling M, Almqvist A. A numerical model for solving three-dimensional rolling contact problems with elastic coating layers. Tribol Lett 2021;69:1–15.
[38] Wang Z, Yu H, Wang QJ. Layer-substrate system with an imperfectly bonded interface: Coupled dislocation-like and force-like conditions. Int J Solids Struct 2017;122:91–109.
[39] Wang Z, Yu H, Wang QJ. Layer-substrate system with an imperfectly bonded interface: spring-like condition. Int J Mech Sci 2017;134:315–35.
[40] Wang Z, Wang W, Wang H, Zhu D, Hu Y. Partial slip contact analysis on three-dimensional elastic layered half space. J Tribol 2010;132(2):021403.
[41] Barber JR. Elasticity. Springer; 2002.
[42] Vijay A, Sadeghi F. Rolling contact fatigue of coupled EHL and anisotropic polycrystalline materials. Tribol Int 2022;107479.
[43] Alfrey T. Non-homogeneous stresses in visco-elastic media. Quart Appl Math 1944;2(2):113–9.
[44] Malvern LE. Introduction to the mechanics of a continuous medium. Monograph, 1969.
[45] Liu SB, Wang QJ. Studying contact stress fields caused by surface tractions with a discrete convolution and fast Fourier transform algorithm. J Tribol 2001;124(1):36–45.
[46] O'sullivan TC, King RB. Sliding contact stress field due to a spherical indenter on a layered elastic half-space. J Tribol 1988;110:235–40.
[47] Chen WT. Computation of stresses and displacements in a layered elastic medium. Internat J Engrg Sci 1971;9(9):775–800.
[48] Carbone G, Putignano C. A novel methodology to predict sliding and rolling friction of viscoelastic materials: Theory and experiments. J Mech Phys Solids 2013;61(8):1822–34.
[49] Brinson HF, Brinson LC. Polymer engineering science and viscoelasticity. springer; 2015.
[50] Christensen RM. Theory of viscoelasticity: an introduction. Elsevier; 1982.
[51] Roylance D. Engineering viscoelasticity, vol. 2139. 2139, Cambridge MA: Department of Materials Science and Engineering–Massachusetts Institute of Technology; 2001, p. 1–37.
[52] Chen WW, Wang QJ, Huan Z, Luo X. Semi-analytical viscoelastic contact modeling of polymer-based materials. J Tribol-Trans 2011;133(4).